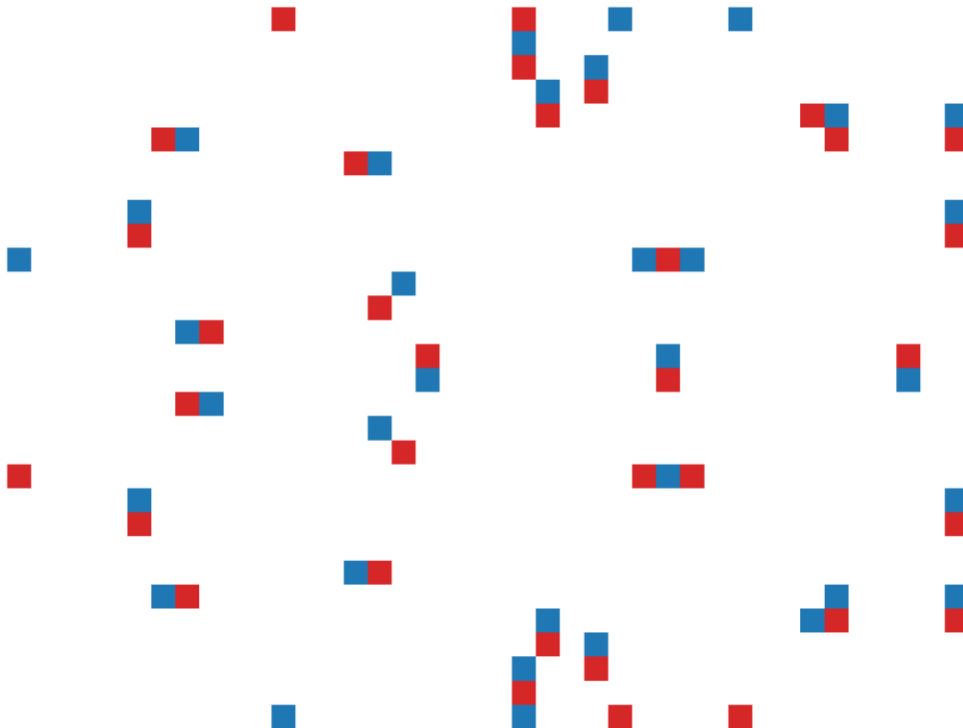


Degree project in Theoretical Physics

Second cycle, 30 credits

2D Coulomb gas simulations of nanowire superconductors

JONATHAN JILG





Master Thesis

2D Coulomb gas simulations of nanowire superconductors

Jonathan Jilg

Department of Physics
School of Engineering Sciences
Royal Institute of Technology, SE-106 91 Stockholm, Sweden

Stockholm, Sweden 2022

Typeset in L^AT_EX

Abstract

A superconducting nanowire single-photon detector (SNSPD) is an emerging, and today commercially available technology, for photon-counting and quantum cryptography. Yet, the photon detection event is not fully understood and current modeling efforts require substantial computational resources which motivates studies of simpler models.

This thesis introduces a model for vortex dynamics in thin-layered superconductors, such as SNSPDs, using a simplified approach, which leads to a 2D Coulomb gas model where the vortices are modeled as electrostatic charges. The model is carefully constructed from the method of images to describe a wire with open boundary conditions and an applied supercurrent. Subsequently, equilibrium and non-equilibrium properties are sampled with the Metropolis-Hastings algorithm and further analyzed and discussed.

The suggested model is shown to be effective and successfully reproduces expected SNSPD behavior; most importantly critical behavior and voltage pulses which are directly measured during detection events. In conclusion, a 2D Coulomb gas model can be a preferred alternative for modeling vortex dynamics in SNSPDs at a small computational cost, motivating further development and studies.

Sammanfattning

Supraledande nanotråd-enfotondetektorer (SNSPD:er) är en framväxande och idag kommersiellt tillgänglig teknologi som används för räknande av fotoner samt inom kvantkryptografi. Ändå är fotondetektionshändelsen inte helt förstådd och de nuvarande modelleringar kräver substantiell datorkraft vilket motiverar studier av enklare modeller.

Det här examensarbetet introducerar en model för vortexdynamik i tunnskiktade supraledare såsom SNSPD:er genom ett förenklat tillvägagångssätt som leder till en 2D Coulombgas-modell där ett vortex modelleras som en elektrisk laddning. Modellen är noggrant konstruerad med öppna randvillkor och den så kallade frysta spegelbildsmetoden samt en pålagd superström. Då samlas mätvärden in på jämvikts- samt icke-jämviktsegenskaper hos systemet som vidare analyseras, jämförs och diskuteras.

Den föreslagna modellen visas vara effektiv och reproducerar framgångsrikt förväntat beteende hos SNSPD:er; framför allt kritiskt beteende och spänningstoppar som direkt uppmäts i en fysisk detektionshändelse. Sammanfattningsvis, kan en 2D Coulombgas-modell vara ett föredraget alternativ för att modellera vortexdynamik hos SNSPD:er för en liten beräkningskostnad, vilket motiverar fler studier av detta.

Acknowledgements

This thesis is the result of one semester of full-time studies at the Department of Physics at the Royal Institute of Technology in Stockholm. I am extremely grateful to my supervisor Prof. Mats Wallin, who first suggested the idea to model SNSPDs with this simplified approach, and his excellent guidance and very generous support during the whole process. Without a doubt, his never-ending anecdotes about Fortran, academia and the history of physics were a constant source of inspiration.

There are of course a countless number of people that have given me invaluable feedback and provided encouragement. A big thank you goes to Mattias Jönsson, Robert Vedin, Jack Lidmar and everyone working with SNSPDs at KTH. I am also grateful for all my teachers during all these years, in particular in my high school Blackebergs gymnasium, who always encouraged me. Likewise, I wish to thank all my colleagues and friends from my exchange semester at ETH, Astronomisk Ungdom, Fysiksektionen and of course Unga Forskare who under all these years provided me the best academic environment one could hope for.

Finally, I wish to thank my relatives and family for their unconditional love, support and belief in me. My parents and my sister Mathilda have always been my rock and cheered me on. I could not have done this without you.

Contents

Abstract	iii
Sammanfattning	iii
Contents	vii
1 Introduction	1
1.1 Models of superconducting nanowire single-photon detectors	2
1.2 Aims of this thesis	3
2 Superconducting nanowires	5
2.1 Stationary Ginzburg-Landau equations	5
2.2 Characteristic length scales	6
2.3 Time-dependent Ginzburg-Landau equations	7
2.4 Vortices	8
2.5 Discretization and the XY model	9
2.6 Toward a simplified model of SNSPDs	10
3 2D Coulomb gas model	13
3.1 Lattice models and the Boltzmann equilibrium	13
3.2 The 2D Coulomb gas from the XY model	14
3.3 Boundary conditions and the method of images	16
3.4 Applied current	17
3.5 Critical current-voltage characteristics	19
4 Monte Carlo method	21
4.1 Overview of Monte Carlo methods	21
4.2 Pair and single insertions	22
4.3 Implementation with Metropolis-Hastings	23
4.4 Python code and data	24

5	Results	25
5.1	Analysis of the potential function	25
5.2	Energy landscapes	28
5.3	Transient analysis	30
5.4	Equilibrium properties	35
5.5	Applied current and non-equilibrium properties	38
6	Summary and conclusions	45
	Bibliography	46

Chapter 1

Introduction

Superconductivity was first discovered by Dutch physicist H. Kamerlingh Onnes when studying electrical conductivity in metals at temperatures close to 0 K. To his surprise, the metals underwent a discontinuous phase transition where electrical resistance suddenly dropped to zero, which was the beginning of extensive research and technological breakthroughs regarding this phenomenon [1, 2]. By some counts, to date 8 Nobel prizes in physics have been awarded to work into superconductivity and the applications include MRI machines, Josephson junctions and sophisticated detectors where even observation of single photons is possible [1, 3].

The origin of superconductivity is quantum mechanical at a microscopic level and can be understood as electrons forming so called Cooper pairs which move with no electrical resistance [1]. These pairs form below a material-dependent critical temperature T_c and are broken for temperatures above this critical value. There are also temperature-dependent critical values for applied current and applied magnetic field which also break superconductivity. Exactly how the applied magnetic field affects the material also defines type I and type II superconductors [1]. At small temperatures, all superconductors are perfect diamagnets, i.e. they expel all magnetic field lines, but for type II the magnetic field may penetrate the material at specific points while still in the superconducting state, which is not true for type I.

One specific emerging superconductor technology is given by Superconducting Nanowire Single-Photon Detectors (SNSPDs) which can detect individual photons. First developed in 2001, it provides efficient count-rate, timing resolution as well as a low dark count (false positives) and is today commercially available for applications in quantum optics and quantum cryptography [4, 5]. Yet, not all details of the detection event are understood and considerable research efforts are currently directed to modeling and simulating the physical effects involved in photon detection.

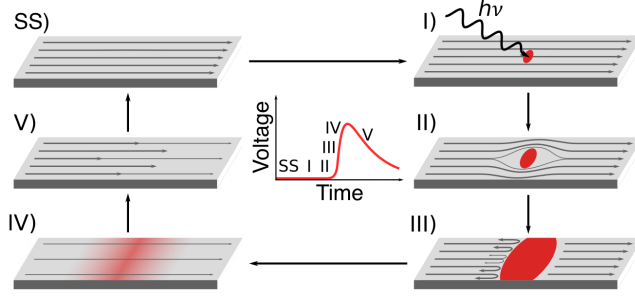


Figure 1.1: Figure on the detection event in an SNSPD. In I to III, photon absorption leads to a local hotspot and creation of vortices resulting in a normal-conducting region. This can be measured as a voltage pulse. The system then relaxes to its superconducting state again. Figure from [6] which is based on the work of [7].

1.1 Models of superconducting nanowire single-photon detectors

The overall research and modeling of SNSPDs is summarized in a topical review [5]. At a fundamental level, an SNSPD is built by a thin superconducting nanowire which is cooled below its critical temperature, usually around the boiling point of liquid helium (4.2 K). The nanowire has a thickness of 5-10 nm, width of 50-100 nm and an unspecified length that is arranged into a compact meandering structure with twists and turns, creating an effective area for photon absorption. A supercurrent is applied in the superconducting wire close to the critical current. This constitutes all essential parts of a photon detector [5].

The mechanisms for a photon detection event is not fully understood at a microscopic level but there are empirical models which account for the experimental findings [5]. The detection event can be visualized in Fig. 1.1. At an overview level, an incident photon becomes absorbed by the nanowire which heats a local area to above the critical temperature, creating a normal-conducting region. This normal-conducting region has a non-zero resistance which affects the passing current giving a measurable voltage pulse. After a short time period, the heat diffuses and the nanowire returns to the superconducting state ready for a new detection. What is not fully understood are the details of how this normal-conducting region influences the superconductivity and gives rise to the voltage pulse.

In particular, superconducting vortices have been identified as a key variable in the detection event [5, 8]. They can be regarded as topological excitations and manifest themselves as regions where an external magnetic field penetrates the superconductor which gives rise to a circulating supercurrent. It should however be noted that vortices may be present even for a zero magnetic field from an applied

current as well as thermal excitations.

Models of SNSPDs usually take the time-dependent Ginzburg-Landau equations or similar variants as their basis. They are nonlinear differential equations that are first order in time and second order in space, which may be integrated with numerical methods. In fact, previous master theses have analyzed these equations and the resulting dynamics of vortices for some geometries [9]. However, there are disadvantages to this approach. These equations introduce many undetermined parameters and the computational cost is highly non-trivial, often requiring implementation on computer clusters. This motivates the study of other possible models which may be more efficient for simulating SNSPDs, which is the topic of this thesis.

1.2 Aims of this thesis

This thesis aims to model and examine vortex dynamics in SNSPDs using a simplified approach which leads to a 2D Coulomb gas model. Unlike other models, this presents a discrete lattice model which may be simulated with Monte Carlo methods at a smaller computational cost. The model is carefully constructed over the course of the thesis with both periodic and open boundary conditions. As will be shown, the latter kind of boundary condition also introduces a need for the frozen mirror image method. Furthermore, a specified supercurrent is applied to the system which directly influences vortex dynamics that generate the voltage pulses observed in SNSPDs.

In the subsequent chapters, details of the model are presented as well as the relevant underlying theory of thin-film superconductors, lattice models and Monte Carlo methods. Simulations were then implemented in Python in order to analyze and compare the transient, equilibrium and non-equilibrium behavior of the model for different parameter choices. The code is provided on Github¹. Of particular interest are critical values for temperature and supercurrent. The overall aim is to compare the models results with experimental properties of nanowire superconductors to assess the validity and usefulness of the model.

¹www.github.com/jonathanjilg/2d-coulombgas

Chapter 2

Superconducting nanowires

There have been many proposed theories to describe superconductors and their physical properties. This chapter provides a brief summary of one of the most successful approaches, the Ginzburg-Landau theory for superconductors, and how the XY model and 2D Coulomb gas model may be derived in the London limit where the magnitude of the so called order parameter is assumed to be constant. The time-dependent Ginzburg-Landau equations are also discussed which are frequently used to simulate superconductors.

2.1 Stationary Ginzburg-Landau equations

First formulated by Vitaly Ginzburg and Lev Landau in 1950, the Ginzburg-Landau (GL) theory provides an empirical description of superconductor physics without the knowledge of its microscopic properties [1]. Only a few years later a microscopic theory was proposed (Bardeen-Cooper-Schrieffer theory) where the Ginzburg-Landau theory could be shown to be a limiting case. The theory describes both type I and type II superconductors.

The GL theory is based on the Landau theory of phase transitions. The free energy of the system is expanded in a series expansion in terms of the order parameter, which is any parameter which changes from a zero to nonzero value during a phase transition [1]. Inspired by this, the GL theory introduces a position-dependent order parameter $\Psi(\mathbf{r}) = |\Psi(\mathbf{r})|e^{i\theta(\mathbf{r})} \in \mathbb{C}$. The order parameter corresponds to the center of mass wavefunction of Cooper pairs and $|\Psi|^2$ gives the Cooper pair density of superconducting electrons [1].

The theory then postulates that the free energy F of a superconducting phase in d dimensions can be expressed as [1]

$$F - F_N = \int d\mathbf{r}^d \left[a|\Psi(\mathbf{r})|^2 + \frac{1}{2}b|\Psi(\mathbf{r})|^4 + \frac{1}{2}c|\nabla\Psi(\mathbf{r})|^2 \right]. \quad (2.1)$$

The free energy of the normal phase is F_N and the parameters a, b and c are parameters which are temperature dependent. Given specific parameter values and minimizing this functional integral with respect to the order parameter Ψ yields the Ginzburg-Landau equations which define the equilibrium state of the superconductor. These differential equations can be formulated, in the case of no external magnetic field, as [1]

$$a\Psi + b\Psi|\Psi|^2 + \frac{1}{2}c\nabla^2\Psi = 0. \quad (2.2)$$

The order parameter Ψ will take on different values depending on the exact values of a and b which are temperature dependent while $c = \hbar^2/(2m_s)$ where \hbar is Planck's constant and m_s the Cooper pair mass. In particular, it is postulated that a changes sign if above or below T_c while $b > 0$ for all T . This usually is expressed as $a(T) = a_0(T - T_c)$ where $a_0 > 0$. The mean-field solution, where Ψ is equal to a constant, is then given by

$$|\Psi|^2 = -\frac{a}{b} = -\frac{a_0(T - T_c)}{b}, \quad (2.3)$$

for $T > T_c$ and $|\Psi|^2 = 0$ otherwise [1]. The phase θ of Ψ here is arbitrary but constant for every position.

2.2 Characteristic length scales

The characteristic length scales in a superconductor are the penetration depth λ and coherence length ξ . They can both be exactly defined in terms of physical constants and parameters in Ginzburg-Landau theory but that will not be discussed here. Instead their interpretations are provided. The penetration depth λ can be seen as how far a magnetic field penetrates the superconductor. For a perfect diamagnet the penetration depth is zero, i.e. $\lambda = 0$, but in practice the magnetic field decays exponentially where λ gives the length at which the magnetic field decreases with a factor $1/e$. The coherence length can be interpreted as the length at which the order parameter Ψ recovers to its mean-field value from a deviation [1]. See Fig. 2.1 for a visual interpretation.

Both length scales are important in the understanding of magnetic vortices. In a vortex, a magnetic field has penetrated the superconductor in a region which will be in normal conducting state where the order parameter $\Psi \approx 0$. The coherence length ξ will then be the radius of this region where Ψ goes from 0 back to its mean-field value. The penetration depth λ gives the length for how far the magnetic field penetrates the superconductor from the vortex. Furthermore, a dimensionless ratio $\kappa = \lambda(T)/\xi(T)$ called the Ginzburg-Landau parameter may be introduced. It can be shown that it is temperature independent and that the value of this ratio determines the type of the superconductor [1]. Type I superconductors have $\kappa < 1/\sqrt{2}$ and type II superconductors have $\kappa > 1/\sqrt{2}$. The difference of these

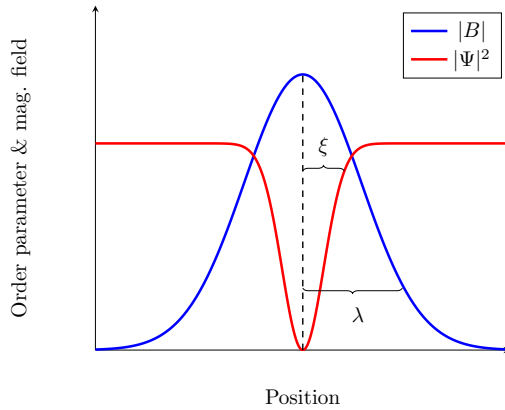


Figure 2.1: Left to right: normal conducting \rightarrow superconducting \rightarrow normal conducting, in terms of penetration depth λ and coherence length ξ . Inside the normal conducting region, the magnitude of the order parameter $|\Psi| = 0$ and $B \neq 0$, and vice versa in the superconducting region. Therefore ξ gives the radius of the normal conducting region and λ the radius of the magnetic penetration.

two types is how they respond to external magnetic fields which is captured in the value of κ , i.e. a relative factor of magnetic field penetration and coherence length.

2.3 Time-dependent Ginzburg-Landau equations

The time-dependent Ginzburg-Landau (TDGL) equations will not be used in this thesis but are shown here for completeness. They were derived by Schmid in 1966 [10] and independently by Gor'kov and Eliashberg [11, 12]. They are nonlinear first-order differential equations in time where the stationary GL equations describe the steady state solution. The validity of these equations are restricted to gapless superconductors, i.e. with many magnetic impurities [13], as well as close to the equilibrium state and near the critical temperature. The equations are

$$\begin{aligned}
 \frac{\hbar^2}{2m_s D} \left(\partial_t + i \frac{e_s}{\hbar} \Psi \right) \psi &= \frac{\hbar^2}{2m_s} \left(\nabla - i \frac{e_s}{\hbar} \mathbf{A} \right)^2 \psi + |\alpha| - \beta |\psi|^2 \psi \\
 \mathbf{j}_s + \mathbf{j}_n &= \frac{1}{\mu_0} \nabla \times (\nabla \times \mathbf{A} - \mu_0 \mathbf{H}) \\
 \mathbf{j}_s &= \frac{\hbar e_s}{2m_s i} (\Psi^* \nabla \Psi - \Psi \nabla \Psi^*) - \frac{e_s^2}{m_s} |\psi|^2 \mathbf{A} \\
 \mathbf{j}_n &= \sigma (-\nabla \Phi - \partial_t \mathbf{A})
 \end{aligned} \tag{2.4}$$

where Φ is the electric potential, D the diffusion constant, σ is the normal conductance and e_s Cooper pair charge [9, 10]. The equations can be shown to be

gauge invariant, i.e. the transformation $\Psi \rightarrow \Psi e^{i\theta(\mathbf{r})}$ and corresponding change of the potentials \mathbf{A}, Φ will also satisfy the same equation.

The TDGL equations are often used to simulate superconductors and vortices [9] and there are also generalized TDGL (GTDGL) equations. However, as seen directly in the equations, there are many undetermined parameters and the gauge invariance introduces a numerical difficulty to obtain a stable solution for all times. The numerical methods therefore involve a substantial computational cost and in practice must be performed on computer clusters. Based on these difficulties, a simpler model that simulates vortex dynamics directly might be preferable, which motivates a closer acquaintance with vortices.

2.4 Vortices

A superconducting vortex or anti-vortex is any circulation of supercurrent around a normal conducting core region, which due to the Lorentz force becomes magnetized [1]. The emergence of vortices is due to local thermal fluctuations as well as external perturbations such as an applied current or applied magnetic field, and this will ultimately transition the superconductor into the normal conducting state. For this reason, an understanding of vortex properties is considered crucial and will give better insight in the superconducting phase transition and the critical temperature, applied field and applied current.

The supercurrent circulation of the normal core induces a local magnetic field whose magnetic flux is quantized. In particular, in type-II superconductors, an external magnetic field may penetrate the superconductor which yields vortices. It has been shown experimentally that the vortices arrange themselves in a lattice called an Abrikosov vortex lattice.

Mathematically, the supercurrent is proportional to the phase gradient $\nabla\theta$ of the complex order parameter. A vortex or anti-vortex can therefore be identified whenever the position-dependent phase around a loop does not average to zero. This can be expressed as

$$\oint d\theta = \oint \nabla\theta(\mathbf{r}) \cdot d\mathbf{r} = 2\pi n, \quad n \in \mathbb{Z}. \quad (2.5)$$

which will always be true for a continuous field. A vortex corresponds to a positive integer n and an anti-vortex corresponds to a negative integer n while $n = 0$ means that the contour encircles vorticity zero, i.e., an equal number of plus and minus quanta. For this reason, the integer n defines the vortex and is called the index or winding number of the vortex.

Based on this classification, vortices can be regarded as topological defects or excitations that cannot be obtained from a continuous transformation of θ [14]. Two vortices with index number ± 1 are illustrated in Fig. 2.3. Similar schematics for higher index vortices can be constructed by making the phase wind more turns for a single rotation.

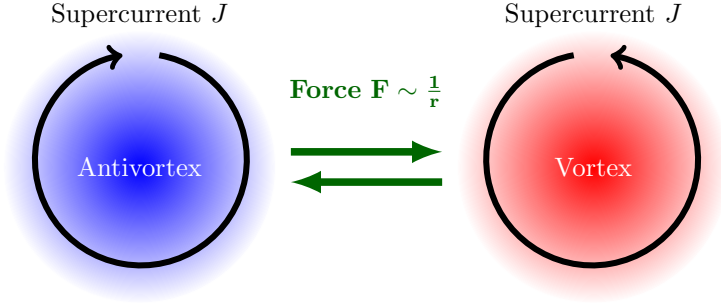


Figure 2.2: Superconducting vortices in terms of the supercurrent J . They act like quasiparticles and interact with the 2D Coulomb potential.

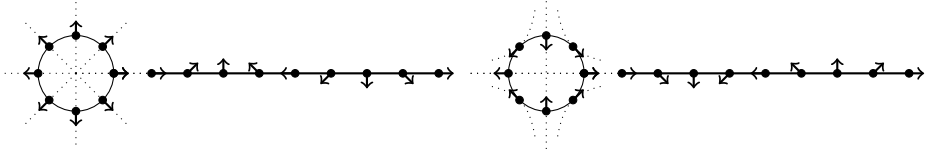


Figure 2.3: A schematic of a vortex (left) and anti-vortex (right) in terms of a field $\theta(\mathbf{r})$. Tracing the circle counter-clockwise, the corresponding vector field also spins counter-clockwise for a vortex and it spins clockwise for an anti-vortex.

In two dimensions, the kinetic energy is approximately

$$H = \frac{1}{2}c \int dr^2 |\nabla \Psi(\mathbf{r})|^2 = \frac{1}{2}c |\Psi|^2 \int dr^2 |\nabla \theta(\mathbf{r})|^2. \quad (2.6)$$

From Eq. 2.5, it follows that $\nabla \theta(\mathbf{r}) = n/r$ and performing the integration gives the following vortex energy

$$H = \frac{1}{2}c |\Psi|^2 \int dr^2 \frac{1}{r^2} = \pi J \ln \left(\frac{L}{a} \right), \quad (2.7)$$

where J is a constant, L the system length and a a cutoff length scale that can be considered to be the vortex core [14]. The self-energy of a vortex would in fact be infinite in this context, in the limit of an infinite system.

2.5 Discretization and the XY model

Assume that $|\Psi|$ is equal to a constant for all positions and time, i.e. the mean field solution. Then, allowing fluctuations in the phase θ over both position and

time, the XY model may be derived for two dimensional systems. In that case, the Hamiltonian is defined as

$$H = \frac{1}{2}c \int d\mathbf{r}^2 |\nabla \Psi(\mathbf{r})|^2 \rightarrow \frac{1}{2}c \sum_{i,j} |\Psi(\mathbf{r}_i) - \Psi(\mathbf{r}_j)|^2, \quad (2.8)$$

where the righthand side is discretized on a lattice. Since $|\Psi(\mathbf{r})| = \text{const}$,

$$\Psi(\mathbf{r}_i) - \Psi(\mathbf{r}_j) = |\Psi| (e^{i\theta(\mathbf{r}_i)} - e^{i\theta(\mathbf{r}_j)}) \quad (2.9)$$

and following some trigonometric algebra, the Hamiltonian is identified as

$$H = \text{constant} - c \sum_{i,j} \cos(\theta_i - \theta_j). \quad (2.10)$$

The value of c will subsequently be set to 1. This Hamiltonian on a lattice defines the well-studied XY model, which can be considered a generalization of the famous Ising model. These are models of ferromagnetism, where spins or magnetic moments at each site are coupled to their neighbours, or other phenomena with the same order parameter symmetry [15].

In two dimensions or higher, the Ising model is known to have a phase transition between an ordered state and disordered state, but the XY model has no phase transition corresponding to symmetry breaking [15]. Instead it is known to possess a Berezinski-Kosterlitz-Thouless transition related to topological excitations in the form of vortices [14]. With this knowledge of vortices and the XY model, it is time to discuss a simpler approach to SNSPDs.

2.6 Toward a simplified model of SNSPDs

The first step toward a simpler model is the assumption that $|\Psi| = \text{const}$ from last section, i.e. the order parameter assumes its mean-field solution for all positions and time. To make the model dynamical, only fluctuations in the phase over time will be allowed while the magnitude remains constant. This still captures a lot of physical aspects in an SNSPD. In particular, vortices are defined exclusively by the phase and a current is expressed as the gradient $\nabla\theta$. The main feature that is lost is the variation and fluctuation of $|\Psi|$, e.g. that $\Psi \rightarrow 0$ near normal conducting regions and the edges of the nanowire.

As discussed in the previous chapter, an SNSPD consists of a thin nanowire which is arranged into a meandering compact structure. The nanowire thickness is of the same order of magnitude as the coherence and penetration lengths ξ and λ and effectively reduces the system to a 2D superconductor, which is henceforth assumed. It should be noted that this is also usually a simplification made for simulations with the TDGL equations.

Now, instead of introducing time-dependent Ginzburg-Landau equations for this simplification, the system can instead be discretized and a Hamiltonian can be

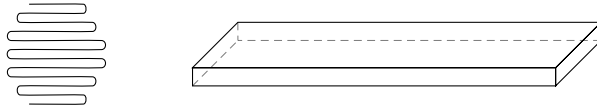


Figure 2.4: A schematic of the compact meandering nanowire structure creating an effective detection area and a close up schematic of the dimensions of the nanowire. The wire is effectively a 2D thin-film.

defined in terms of the phase θ . This directly leads to the XY model, a discrete lattice model, which may be simulated with Monte Carlo methods. The vortices of this model may however be simulated explicitly by the 2D Coulomb gas model, as will be discussed in the next chapter.

Before moving on, let us ask the important question how this models an SNSPD. The assumed simplifications leave only phase θ fluctuations which is the only information needed to define vortices and currents. A current bias, which is needed in the nanowire, can then be implemented as a specified phase gradient or directly as a Lorentz force on the vortices. The boundary conditions also need to be specified. For the XY and Coulomb gas models, periodic boundary conditions are usually applied but in this case boundary effects are important. In particular, no current should cross the wire edges. This introduces a need for open boundary conditions and the method of images in electrostatics, i.e. mirror systems of opposite charge should be introduced at each boundary. This ensures that no current passes the edge.

Summary of the modeling approach in this thesis

1. Assume that the system has two spatial dimensions.
2. Minimize the free energy of the Ginzburg-Landau theory to get the mean field value of $|\Psi|$ as a function of temperature T .
3. Add phase fluctuations θ by defining a new model with $|\Psi| = \text{constant}$ and $H = \int |\nabla \Psi|^2 dr^2$.
4. Discretize H and get the XY model. Impose applied current as a phase gradient and boundary conditions with the method of images in electrostatics.
5. To simulate vortices directly, derive the 2D Coulomb gas model from the XY model and translate boundary conditions and applied current for this model.

Chapter 3

2D Coulomb gas model

In this section, the fundamental theory of lattice models and Boltzmann equilibrium is shortly summarized, in particular how internal energy, heat capacity and critical exponents are defined, which will be used later. Then the XY model is used to derive the 2D Coulomb gas model which explicitly models vortices as electrical charges on a lattice. Details of this Hamiltonian and potential are specified to get a well-defined model. Then, an applied supercurrent is incorporated as well as boundary conditions where the method of images is used. Finally, expected critical behavior of non-linear current-voltage characteristics is discussed and derived for the model, which will be of interest in the simulation results.

3.1 Lattice models and the Boltzmann equilibrium

Any regular discretization of a continuous physical model leads to a lattice model which may be easier to study both analytically and numerically. In statistical physics, the properties of equilibrium lattice models have been studied extensively, for instance the Ising and XY model [15]. In particular, both models exhibit phase transitions in the thermodynamic limit at the critical temperature T_c . The following summary is based on the theory of statistical mechanics presented in [15].

At equilibrium these models follow the Boltzmann distribution which means that the probability of finding a particular configuration is proportional to its Boltzmann factor $\exp(-\beta H)$ where $\beta = 1/(kT)$ is the inverse temperature, k the Boltzmann coefficient and H the energy of the configuration. The sum of the Boltzmann factors defines the partition function

$$Z = \sum_{\{s_i\}} e^{-\beta H_{\{s_i\}}} \quad (3.1)$$

where the summation is over all possible configurations $\{s_i\}$. It can be shown that determining Z as a function of all relevant parameters completely defines all thermodynamic properties of the model such as the internal energy U , heat capacity c and entropy S [15].

The number of possible configurations can easily be larger than the number of particles in the universe, even for small systems, which means that calculating Z directly is not feasible. Instead, as will be discussed in the next chapter, Z and other thermodynamic quantities can be sampled by Monte Carlo methods, simulating the thermal fluctuations. Furthermore, calculating the internal energy U from the partition function Z for instance, requires derivatives which amplify the noise in the sampled data. For this reason, the energy H and the order parameter Ψ , phase θ or number of vortices n are usually sampled directly in a numerical simulation.

The other relevant quantities can be calculated directly from the sampled energy H and other measured quantities. The heat capacity is calculated as

$$c = \frac{\langle H^2 \rangle - \langle H \rangle^2}{NT^2}, \quad (3.2)$$

where N is the number of samples and $\langle Q \rangle = \sum Q \exp(-\beta H)$ denotes an expectation value of the quantity Q . The entropy can then be calculated as the integral

$$S(T) = \int_0^T \frac{c}{T'} dT', \quad (3.3)$$

and the free energy F from the entropy by the relation

$$F = U - TS = \langle H \rangle - TS. \quad (3.4)$$

Near the critical temperature T_c , critical behavior is observed where physical quantities can be seen to follow universal power law divergences and relationships. The particular exponents describing the power law divergences are known as *critical exponents* which are not dependent on the particular geometry of the system. For example, the characteristic length scale $\xi \sim |t|^{-\nu}$ (if symmetry breaking occurs) where ν is a particular critical exponent and $t = |(T - T_c)/T_c|$ the reduced (non-dimensional) temperature [15].

3.2 The 2D Coulomb gas from the XY model

A vortex in the XY model may be defined as the integer winding number

$$n = \frac{1}{2\pi} \oint \nabla \theta(\mathbf{r}) \cdot d\mathbf{r}, \quad (3.5)$$

which is approximated to a finite sum over a plaquette (the smallest closed loop in the lattice) in the XY model. As discussed, $n > 0$ corresponds to a vortex

and $n < 0$ to an anti-vortex (and $n = 0$ to no vortex). However, vortices may be modelled explicitly by a duality transformation and change of variables leading to the Coulomb gas model. Details of this derivation are omitted, but may be found in for example [16, pp. 399–405].

In the 2D Coulomb gas model, vortices are modelled as electric charges q_i on a lattice. All charges attract or repel all other charges by the 2D Coulomb force which is proportional to $1/r$ ($-\ln(r)$ for the potential) where r is the separation distance. The ground state is the vacuum state where $q_i = 0$ at all lattice sites, corresponding to total energy 0. Non-zero charges therefore show up as excitations when the temperature is sufficiently high, corresponding to the Berezinski-Kosterlitz-Thouless transition.

The partition function of the 2D Coulomb gas may be written as

$$Z_{CG} = \prod_i \sum_{q_i=0,\pm 1,\pm 2,\dots} \exp(-\beta H_{CG}), \quad (3.6)$$

which is a sum over an infinite number of possible states, even for a finite system size. The Hamiltonian H_{CG} is a sum over all pairwise interactions

$$H_{CG} = \frac{1}{2} \sum_{i,j} q_i q_j V(r_{ij}), \quad (3.7)$$

where V is the 2D Coulomb potential in a lattice and r_{ij} is the distance between sites i and j . For a continuous system $V \sim -\ln r$ but for a lattice, this does not hold exactly. It can be shown that for a lattice [17], this potential is defined as the Fourier series

$$V(\mathbf{r}) = \frac{1}{L^d} \sum_{\mathbf{k}} e^{i\mathbf{r}\cdot\mathbf{k}} V(\mathbf{k}), \quad V(\mathbf{k}) = \frac{2\pi}{4 - 2\cos(k_x) - 2\cos(k_y) + \lambda^{-2}}, \quad (3.8)$$

where λ can be identified as an effective screening length. Any finite λ gives a finite self energy of a single vortex as $\frac{1}{2}q^2V(0) < \infty$ and for $\lambda = \infty$ the self energy diverges. In this case, the self energy of a single vortex is subtracted from the total energy which then will remain finite. It should be noted that a previous thesis has studied the effect of λ in a renormalization group context, where it was found that both $\lambda < \infty$ and $\lambda = \infty$ give similar results, with some differences in the efficiency of the simulation [18].

The Monte Carlo method to simulate this model will be fully described in Ch. 4 but is based on vortex-antivortex pair insertion at random sites. In preparation, some useful results and important details will be discussed here, particularly calculations of energy changes ΔH .

It should be emphasized that the Hamiltonian H_{CG} considers all pairwise interactions and not only nearest neighbour interactions as in the Ising and XY models. For this reason calculating H_{CG} is of the order $\mathcal{O}(V^2) = \mathcal{O}(L^4)$ where $V \sim L^2$ is

the volume and L is the system length size. To simulate this system, all energy calculations will have to be optimized since this will have the greatest computational cost.

Insertion of dq at (x_a, y_a) which has charge q_a and $-dq$ at (x_b, y_b) which has charge q_b leads to the following changes,

$$\begin{aligned} q_a &\rightarrow q'_a = q_a + dq \\ q_b &\rightarrow q'_b = q_b - dq \\ q_i &\rightarrow q'_i = q_i, \quad i \neq a, b \end{aligned} \tag{3.9}$$

$$H = \frac{1}{2} \sum_{i,j} q_i q_j V(r_{ij}) \rightarrow H' = \frac{1}{2} \sum_{i,j} q'_i q'_j V(r_{ij}).$$

The resulting energy change $\Delta H = H' - H$ may then be calculated as

$$\begin{aligned} \Delta H &= \frac{1}{2} \left[(q_a + dq)^2 - q_a^2 + (q_b - dq)^2 - q_b^2 \right] V(0) \\ &\quad + [(q_a + dq)(q_b - dq) - q_a q_b] V(1) \\ &\quad + \frac{1}{2} \sum_{i \neq a, b} dq (q_i V(r_{ai}) - q_i V(r_{bi})), \end{aligned} \tag{3.10}$$

which may be written as

$$\begin{aligned} \Delta H &= (V(0) - V(1)) (q_a - q_b + dq) dq \\ &\quad + \sum_{i \neq a, b} q_i dq (V_{ai} - V_{bi}). \end{aligned} \tag{3.11}$$

This calculation has computational cost $\mathcal{O}(V) = \mathcal{O}(L^2)$ which is much better than calculation of the total Hamiltonian.

3.3 Boundary conditions and the method of images

In this thesis, two geometries are considered: a film geometry with periodic boundary conditions (PBC) and a wire geometry with open boundary conditions (OBC) in y and PBC in x . PBC are a natural choice in lattice models since they reduce both boundary and finite size effects of the model. However, for a nanowire, this will not do, vortices are in fact attracted to the boundaries analogously to electric charges in conductors. The boundary effects are therefore important and the physical condition is that no current should flow over the edge (Neumann condition). To impose this, a mathematical trick is introduced: the method of images from electrostatics. For every charge q at (x, y) , there will be a corresponding mirror charge $-q$ at $(x, -y)$.

The derivation of the energy change is similar to the previous calculation, but this time four charges are involved q_a, q_b, q_c, q_d where $q_c = -q_a$ and $q_d = -q_b$ are mirror charges (see Fig. 3.1). The relevant quantities are now

$$\begin{aligned}
 q_a &\rightarrow q'_a = q_a + dq \\
 q_b &\rightarrow q'_b = q_b - dq \\
 q_c &\rightarrow q'_c = q_c - dq \\
 q_d &\rightarrow q'_d = q_d + dq \\
 q_i &\rightarrow q'_i = q_i, \quad i \neq a, b, c, d
 \end{aligned} \tag{3.12}$$

$$H = \frac{1}{2} \sum_{i,j} q_i q_j V(r_{ij}) \rightarrow H' = \frac{1}{2} \sum_{i,j} q'_i q'_j V(r_{ij}).$$

Then, going through the necessary calculations, the result can be expressed as

$$\begin{aligned}
 \Delta H &= 2V_0 [1 + dq [q_a - q_b]] \\
 &+ 2 [(-q_a + q_b) dq - 1] V_{ab} \\
 &+ [-2q_a dq - 1] V_{ac} + [2q_b dq - 1] V_{bd} \\
 &+ [(q_a - q_b) - 1] V_{ad} + [(q_a - q_b) - 1] V_{bc} \\
 &+ dq \sum_{i \neq a, b, c, d} q_i [V_{ai} - V_{bi} - V_{ci} + V_{di}].
 \end{aligned} \tag{3.13}$$

The change of energy for a single vortex insertion (see Fig. 3.2) for a mirror configuration is the same expression as before for pair insertion, i.e.

$$\begin{aligned}
 \Delta H &= (V(0) - V(1)) (q_a - q_b + dq) dq \\
 &+ \sum_{i \neq a, b} q_i dq (V_{ai} - V_{bi}).
 \end{aligned} \tag{3.14}$$

3.4 Applied current

An applied supercurrent in the x direction gives rise to a Lorentz force on the vortex, driving movement in the y direction. For this reason, an energy change corresponding to vortex y displacement should be included, proportional to the supercurrent J . This can be expressed as

$$\Delta H_{\text{current}} = J dq (y_2 - y_1) = \pm J, \tag{3.15}$$

depending on the specific values on y_1, y_2 and dq (see Fig. 3.2). As an example, vortex pair insertion at (x, y) and $(x, y + 1)$ gives $\Delta H_{\text{current}} = J$ (if $dq = 1$) while insertion at (x, y) and $(x + 1, y)$ gives $\Delta H_{\text{current}} = 0$.

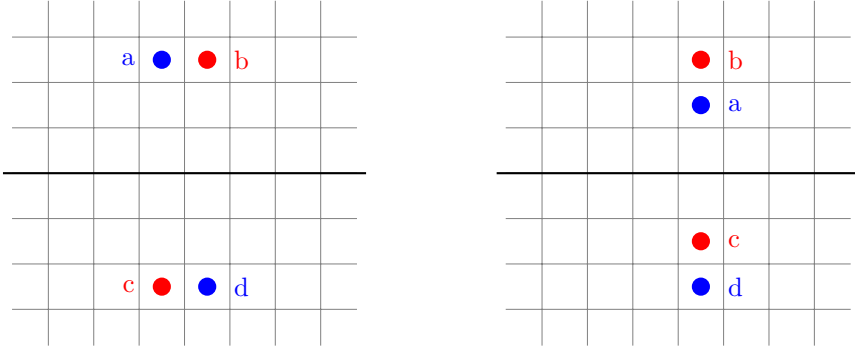


Figure 3.1: Vortex pair insertion with mirror configuration.

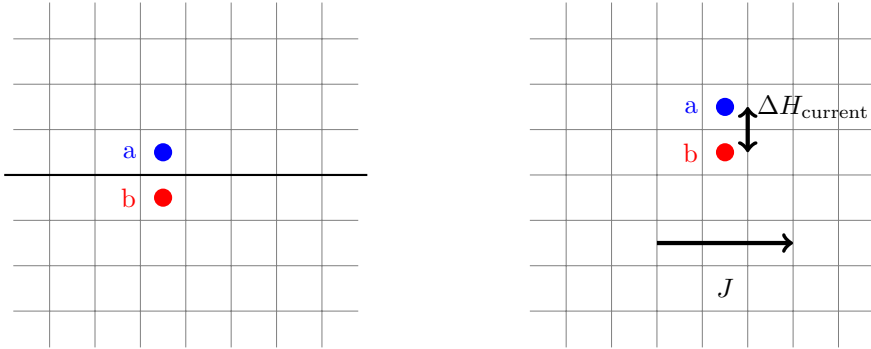


Figure 3.2: Left panel: Single vortex insertion with mirror configuration. This insertion is only performed at the boundary. Right panel: An applied supercurrent J in the x direction induces a particle flow in the y direction.

The applied current is expected to induce a vortex flow in the y direction which may be defined as

$$dQ_y = dq(y_2 - y_1) = \pm dq, \quad (3.16)$$

for any Monte Carlo step. Summing these over all Monte Carlo steps give the total $Q_y(t)$ as a function of time. The voltage V may then be calculated as

$$V = \frac{h}{2e} \frac{dQ}{dt}, \quad (3.17)$$

where h is Planck's constant and e the electron charge.

It should be noted that the Hamiltonian H becomes path-dependent in this model with an applied current, i.e. the energy H will no longer be only dependent on the vortex configuration. The energy will actually be different for a single vortex at $y = y_0$ depending on if it was inserted at $y = 0$ or $y = L - 1$ and moved to $y = y_0$. The respective energies are $e + (y_0 + 1)\Delta H_{\text{current}}$ and $e + (L - y_0)\Delta H_{\text{current}}$ with the self energy e . This only means that a term is missing in H . In Ginzburg-Landau theory and the XY model it is possible to introduce an applied current and get an energy of a particular configuration. This information is however lost when only considering vortices but is at the same time recovered when adding the term $\Delta H_{\text{current}}$ to the overall energy change ΔH .

3.5 Critical current-voltage characteristics

In this section, a scaling argument for the non-linear current-voltage characteristic near T_c is presented [19]. As before, ξ denotes the characteristic length scale, A the magnetic vector potential and f the free energy density. The critical behavior follows the power laws

$$\ln \xi \sim |t|^{-1/2}, \quad A \sim \xi^{-1}, \quad f \sim \xi^{-d}, \quad (3.18)$$

where $t = (T - T_c)/T_c$ is the reduced temperature, and d the number of spatial dimensions. Following this, the critical behavior of the electric field E can be derived from Maxwell's equations and the current density from Ginzburg-Landau theory,

$$\begin{aligned} E &\sim \frac{dA}{dt} \sim \frac{\xi^{-1}}{\xi^z} = \xi^{-(z+1)} \\ J &\sim \frac{df}{dA} \sim \frac{\xi^{-d}}{\xi^{-1}} = \xi^{-(d-1)}. \end{aligned} \quad (3.19)$$

This implies that the quantity $J\xi^{d-1}$ is scale invariant near T_c and that

$$E = \xi^{-(z+1)} G(J\xi^{d-1}) \quad (3.20)$$

where G is a scaling function. For finite systems, there will also be a finite size effect so another argument is passed to G according to

$$E \sim \xi^{-(z+1)} G(J\xi^{d-1}, L/\xi) \sim L^{-(z+1)} G(JL^{d-1}, L/\xi) \sim J^3, \quad (3.21)$$

for $z \approx 2$ and $d = 2$.

Now, a physical argument can be made for a power law form of the IV -characteristic. For large currents, the system should be insensitive to the exact value of T . The Lorentz force induced by the current drives the system out of equilibrium and the equilibrium fluctuations are replaced by a driven non-equilibrium evolution. Therefore the diverging characteristic length ξ must drop out of the expression for large currents which is achieved if

$$G(x) = x^{(z+1)/(d-1)} \implies E = J^{(z+1)/(d-1)}. \quad (3.22)$$

The relation between E and J defines the expected nonlinear IV -characteristic for large currents near T_c . The value of T_c may therefore be estimated from data curves for the IV -characteristics where the curve changes.

Chapter 4

Monte Carlo method

This chapter explains the Monte Carlo methods used to simulate the 2D Coulomb gas model. Firstly, a brief overview is given to the theoretical background of Monte Carlo methods where it is shown that the implementation satisfies both ergodicity and the detailed balance equation. The details of the implementation are then described step-by-step and the code as well as data analysis is provided on Github below.

4.1 Overview of Monte Carlo methods

Monte Carlo methods account for one of the largest and most important type of numerical methods used in statistical physics. Based on a sampling approach, the fundamental idea is to simulate a system undergoing thermal fluctuations to estimate properties of that thermal system [15]. The mathematical starting point is to introduce a so called Markov process which means to randomly generate a new state ν given a state μ with a certain probability $p(\mu \rightarrow \nu)$. It is also required that this probability does not change over time and that p only depends on μ and ν [15].

In order to sample a thermal system obeying the Boltzmann distribution, some conditions must be met. The first condition is that the method must be *ergodic* which in this context means that given a state μ , any other state ν should be reachable in a finite time. In addition, the method must obey the balance equation

$$\frac{p(\mu \rightarrow \nu)}{p(\nu \rightarrow \mu)} = e^{-\beta(E_\nu - E_\mu)} \quad (4.1)$$

which ensures that the system will equilibrate to the Boltzmann distribution [15].

The numerical method in this thesis uses the Metropolis-Hastings algorithm which is one of the most famous and used Monte Carlo algorithms [20]. It is a single-flip algorithm which selects a random site, calculates the resulting energy

change and accepts the flip if the change in energy is negative or with probability $e^{-\beta\Delta H}$ if it is positive.

The Metropolis algorithm is usually effective but not the best choice near the critical region. There, a phenomenon known as *critical slowing down* occurs where the correlation time τ in the system diverges as $T \rightarrow T_c$. The divergence can be expressed in a power law $\tau \sim L^z$ where z is the dynamic exponent. It is not specific nor universal to a model but rather depends on the algorithm. For the Metropolis algorithm, $z \sim 2$ which greatly impacts its performance near the critical temperature [15].

4.2 Pair and single insertions

For the film geometry (PBC), the implementation is straight-forward where a single flip accounts for a vortex-antivortex pair insertion; i.e. two neighbouring sites are randomly selected. At the first site, $q_1 \rightarrow q_1 + dq$ is proposed and at the second $q_2 \rightarrow q_2 - dq$ which gives a resulting energy change ΔH which gives a certain acceptance probability. It can be shown that the Metropolis algorithm satisfies the detailed balance equation [15] and since vortex-antivortex insertions may change any neutral configuration to any other, it is ergodic. If charged configurations are allowed, single vortex insertion is also implemented which may give any configuration.

In principle, one should try single vortex insertion if the self-energy of a single vortex is finite, i.e. $\lambda < \infty$ in the calculation of the potential V . This is however not implemented since the associated energy is very large and would not be excited for normal temperature ranges, and, furthermore, this is only an issue for PBC. For the wire geometry (OBC), there will always be an opposing charge in the mirror system so the energy will never diverge. Disregarding single vortex insertion for PBC is therefore an approximation that will have minimal impact on the results.

The implementation for the mirror 2D Coulomb gas model is the same with certain key differences. Sites for pair or single insertions are only selected in the physical system and the mirror sites are updated to always be their mirror images. This means that a pair insertion changes four sites and a single insertion changes two sites. The energy calculations are changed accordingly as specified in last chapter. The detailed balance condition still applies as does ergodicity. Of course, this only holds for the ‘physical’ part of the lattice, if one considers the entire lattice only mirrored configurations are allowed.

It should be mentioned that the energy calculations are the most computationally demanding in the 2D Coulomb gas due to the global interaction of vortices. In the Ising model for instance, energy interactions are only between neighbours which greatly simplifies the calculations which are of order $\mathcal{O}(1)$ while the Coulomb gas are of the order of the system size, i.e. $\mathcal{O}(L^2)$ after simplification.

4.3 Implementation with Metropolis-Hastings

The general outline of the Metropolis-Hastings algorithm implemented for the 2D Coulomb gas model is the following.

1. Try vortex-antivortex pair insertion at a random location
2. Calculate the resulting change in energy ΔH of the proposed pair insertion.
3. Accept if $\Delta H \leq 0$ or with probability $e^{-\beta\Delta H}$. Reject otherwise.
4. If accepted, change to the new proposed lattice configuration and update values.
5. Repeat.

These steps are iterated and measurements on quantities such as E are measured during the run of the experiment. Further details of these steps are provided below.

Before any of these steps, an array of zeros with size $L_x \times L_y$ is created representing the system configuration. This corresponds to the vacuum state with no vortices. A potential V is tabulated based on the system lengths L_x and L_y as a Fourier sum according to the formulas in the last chapter. The penetration depth λ is chosen with a specific value. For the wire geometry (OBC), the lattice has size $L_x \times 2L_y$ which is used to tabulate the corresponding potential.

The first step in the algorithm starts by selecting a random lattice site (i, j) and a random neighbour of this site $(k, l) = (i \pm 1, j \pm 1)$. If the boundary conditions are periodic L is identified by 0 and -1 is identified by $L - 1$. If the boundary conditions are not periodic (i.e. open), this proposed configuration is discarded and the process starts over.

For these random sites, the proposed configuration change for the film geometry (PBC) is then $q_{ij} \rightarrow q_{ij} + dq$ and $q_{kl} \rightarrow q_{kl} - dq$ where $(k, l) = (i \pm 1, j \pm 1)$. The proposed change in charge $dq = \pm 1$ is selected at random with equal probability. For the wire geometry (OBC), the method of images is applied to the model, and the mirror charges will be updated as well according to $q_{i'j'} \rightarrow -q_{ij} - dq$ and $q_{k'l'} \rightarrow -q_{kl} + dq$ where the primes denote the mirror locations. These mirror coordinate sites can be determined to be $(i', j') = (i, 2L_y - 1 - j)$ for a mirror in y .

For the second step, the energy change ΔH is calculated by the aforementioned formulas from last chapter, i.e.

$$\begin{aligned}
 \Delta H = & 2V_0 [1 + dq [q_a - q_b]] \\
 & + 2 [(-q_a + q_b) dq - 1] V_{ab} \\
 & + [-2q_a dq - 1] V_{ac} + [2q_b dq - 1] V_{bd} \\
 & + [(q_a - q_b) - 1] V_{ad} + [(q_a - q_b) - 1] V_{bc} \\
 & + dq \sum_{i \neq a, b, c, d} q_i [V_{ai} - V_{bi} - V_{ci} + V_{di}],
 \end{aligned} \tag{4.2}$$

where a denotes site (i, j) , b the site (k, l) and c and d the mirror sites. As mentioned, this part is the most costly of the simulation.

The next step tests if $\Delta H \leq 0$ and if true the move is accepted. If false, i.e. $\Delta H > 0$, a random number r is generated and the move is accepted if $r < \exp(-\beta\Delta H)$. For accepted moves, the configurations are updated and quantities are measured before repeating this loop again and again. In order to compare systems with different sizes, a sweep is defined to be $L_x L_y$ loops of these steps.

4.4 Python code and data

The implementation was done and tested in Python 3.10.1 with NumPy, Numba and Matplotlib. The code alongside with data and figure generation is available on www.github.com/jonathanjilg/2d-coulombgas.

Chapter 5

Results

The results of the simulations are presented in this chapter for both film and wire geometries. In particular, the results are divided into separate sections; starting with energy landscapes of the model, then moving on to an analysis of the transient behavior of the model and finally looking into detail of the equilibrium and non-equilibrium properties. All raw data and figures are made available on www.github.com/jonathanjilg/2d-coulombgas.

5.1 Analysis of the potential function

The potential function V determines all energy calculations and hence the Monte Carlo dynamics. It is therefore important to understand all details of its properties, necessary approximations and the effects of parameters and system size.

In Fig. 5.1, the potential V is shown for $L = 16$ and $\lambda = 4L$. It is indexed by x and y distances (both positive integer quantities) and was constructed with a truncated Fourier series as discussed in previous chapter. As illustrated, there is a steep descent close to $(0, 0)$ and a local minimum at $(0.5L_x, 0.5L_y)$. The function is periodic with period L which explains the peaks at the edges. This would describe a potential in an $L \times L$ system since the maximum x and y distances between two sites would be $L/2$, respectively. The potential can also be constructed with a larger period than L .

A cross section of the V gives a clearer picture how the potential V varies over the system (Fig. 5.2). For $\lambda = 4L$, the potential V is in the range 100 to 105, and the difference between the largest and lowest value of V is smaller than 5 for all L and λ . However, increasing the screening length factor $a = \lambda/L$, shifts this range while keeping the overall shape intact, for large enough values of a (Fig. 5.2). Regardless, the potential shift only affects the self energy of single vortices, all pair configurations will only depend on relative differences in V . In practice, an integer $a > 1$ seems to be sufficient for the potential. In this thesis, we will use $\lambda = 4L$.

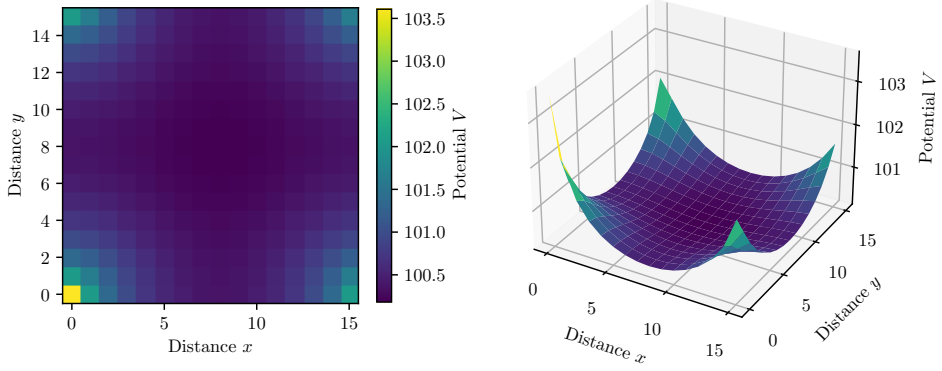


Figure 5.1: The 2D Coulomb potential V constructed by a Fourier sum with period L for $L = 16$ and $\lambda = 4L$.

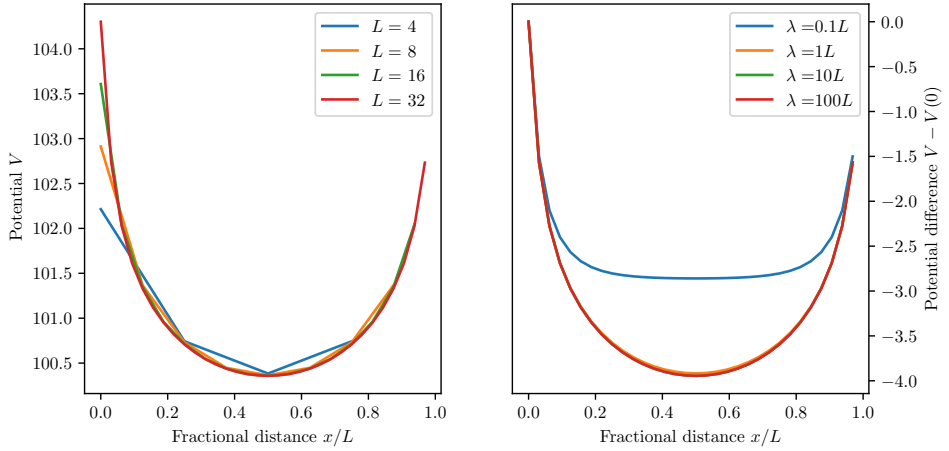


Figure 5.2: The 2D Coulomb potential V constructed by a Fourier sum with period L as a function of x/L for different system lengths L (right panel: $L = 64$) and penetration depths λ at a constant $y = 0$ (left panel: $\lambda = 4L$). The same curve is obtained changing x and y .

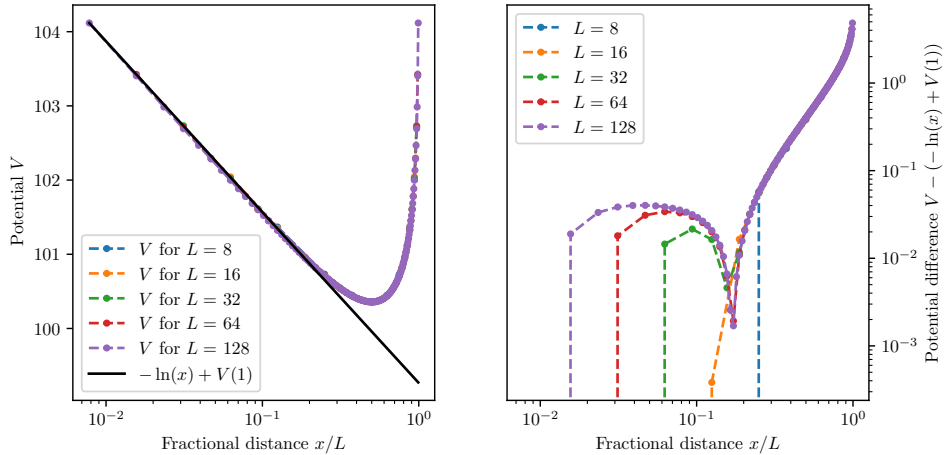


Figure 5.3: Comparison of $-\ln(x)$ and The 2D Coulomb potential V in a semilog plot. As before, V is constructed by a Fourier sum with period L as a function of x/L for different system lengths L and penetration depth $\lambda = 4L$ at a constant $y = 0$. The same curve is obtained changing x and y .

The potential V is also expected to show logarithmic behavior, i.e. $V \sim -\ln(x)$ in the limit $L \rightarrow \infty$. Indeed, a plot on a logarithmic scale shows this agreement until around $x/L = 0.2$ where the difference increases (Fig. 5.3). This is entirely due to V being periodic with period L . Interestingly, in the limit $L \rightarrow \infty$, the potential difference between V and $-\ln(x)$ approaches a constant for $x/L < 0.2$ (Fig. 5.3). However, as previously said, all relevant energy calculations only depend on relative differences in the potential and are unaffected by a constant shift.

To further discuss the effects of the potential shift introduced by λ , it is insightful to calculate the self energy of a single vortex and pair energy of a vortex-antivortex pair in terms of the potential. From Eq. 3.10, the self energy is $V(0)/2$, which quantifies an absolute potential scale, and the pair energy is $V(0) - V(1)$ which quantifies a relative potential scale. In Fig. 5.4, $V(0)/2$ increases for both L and λ , which is expected. The self energy should diverge for infinite systems. In comparison, the pair energy is in a narrow range between 1.46 and 1.57 (dimensionless), which is only slightly affected by the choice of λ . Interestingly, the pair energy for $L = 128$ was found to be 1.5704 which is a close lower bound to $\pi/2 = 1.5708$.

The Fourier period of the potential is also an important factor. By construction, this implementation with Fourier period L gives the periodic continuation of $\ln r$ which corresponds to the series $\sum_n -\ln(|nL - x|)$. Choosing another period length, the shape of V changes accordingly and in particular, relative potential differences are decreased for smaller periods (Fig. 5.5). In contrast, as the period factor, i.e. the ratio $a = \lambda/L$, increases, the potential gets closer to $-\ln(x)$, as expected (Fig.

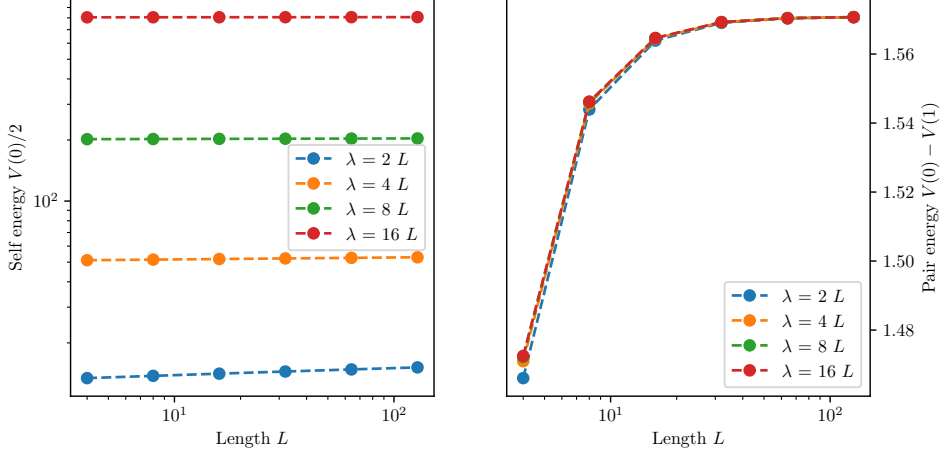


Figure 5.4: The self energy and pair energy for expressed in the potential V for different system lengths L and penetration depths λ . For $\lambda, L \rightarrow \infty$, the self energy is expected to diverge.

5.5). The validity of a period length L can be confirmed by a direct comparison with the series $\sum_n -\ln(|nL - x|)$ and the constructed V . The difference of the two converges to a constant, see Fig. 5.6, which represents a constant shift. In this thesis, we will use a Fourier period of L .

5.2 Energy landscapes

From the potential V , any energy configuration can be calculated. There are an infinite number of possible configurations but single and pair vortices are of particular interest. For PBC, the energy cost of both single and pair insertion are not position dependent, but for OBC the energy will be dependent on the distance to the mirror. As seen in Fig. 5.8, the energy of a single vortex is close to 1.57 near the mirror and increases up to 4.0 in between the mirrors. In contrast, the energy for a vortex pair is approximately constant around 3.14 which is reduced to 2.3 at the edges. The vacuum state with no vortices has 0 energy. It should be noted that these energies are approximately a factor 2 larger than for the system with periodic boundary conditions. This is also seen for the energy cost to separate a vortex-antivortex pair (Fig. 5.7), which means that vortex-antivortex pairs will be more strongly bound at the same temperatures.

This is not the full picture, since the applied current also affects the energy landscape. The energy then also depends on the particular path of a single vortex, as previously discussed. Then the current either gives a negative or positive contribution to the overall energy depending on the charge q of the vortex and sign

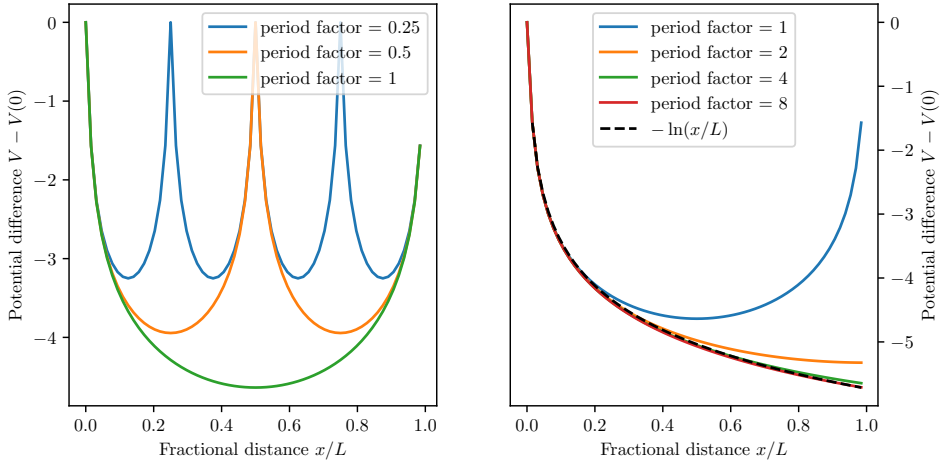


Figure 5.5: A comparison of the potential V for different period factors, i.e. the period of the Fourier sum. The penetration depth $\lambda = 4L$ and $L = 64$ were used here. As the period factor increases, the potential gets closer to $-\ln(x)$.

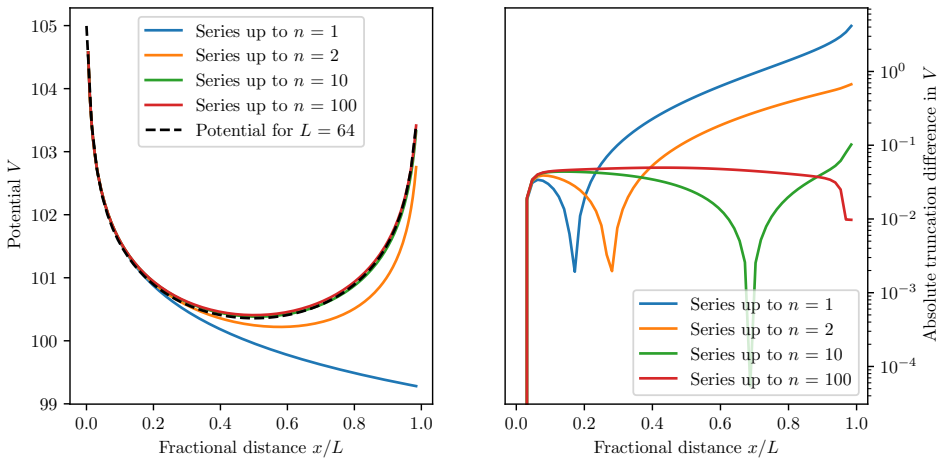


Figure 5.6: The potential with a period factor equal to 1, compared to the series $\sum_n -\ln(|nL - x|)$ which has the same Fourier coefficients. The penetration depth $\lambda = 4L$ and $L = 64$ were used here. It can be seen that the difference between the series and the potential approaches a constant.

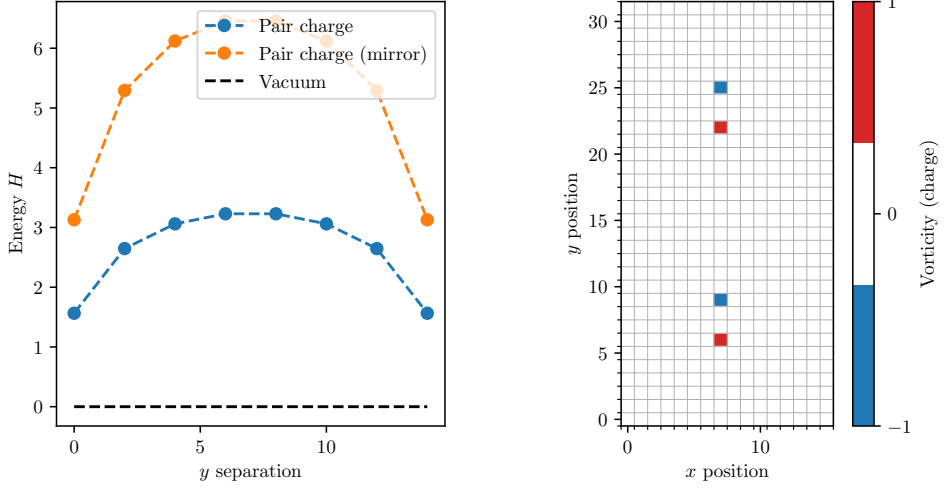


Figure 5.7: Left panel: The energy cost separating vortex-antivortex pairs (both mirror and non-mirrors) given a separation distance y for system length $L = 16$, penetration length $\lambda = 4L$ and Fourier period L . Right panel: mirror configuration used to generate the energy in left panel with y separation 3. A vortex-antivortex pair is inserted at $(x, y) = (7, 7)$ and $(7, 8)$ and step-wise separated.

of the supercurrent J . A negative contribution favors vortex movement across the system and it is seen that a supercurrent of $J_c = 1.57$ gives a negative energy for all positions, indicating that this is the supercurrent at $T = 0$ (Fig. 5.9). J_c is expected to decrease for larger T .

5.3 Transient analysis

Here Monte Carlo (MC) data is presented as well as an analysis of the transient behavior. A first look at the initial sweeps (a sweep is $L_x L_y$ MC steps, which scales with the system size) of both PBC and OBC (Figs. 5.10, 5.11) shows that for high enough temperatures T , vortex pairs are inserted. As seen, there is a transient involved which cannot be determined visually by a few sweeps. Instead this will be analyzed further.

The transient curves for the energy (Fig. 5.12) and particle flow Q_y (Fig. 5.13) for different temperatures show that the data is very noisy, giving large fluctuations in H . However, it can be seen visually that the transient is 100-200 sweeps at maximum. This analysis could be improved by a computation of the correlation time, but instead the first 1000 sweeps are discarded as a transient, ensuring that

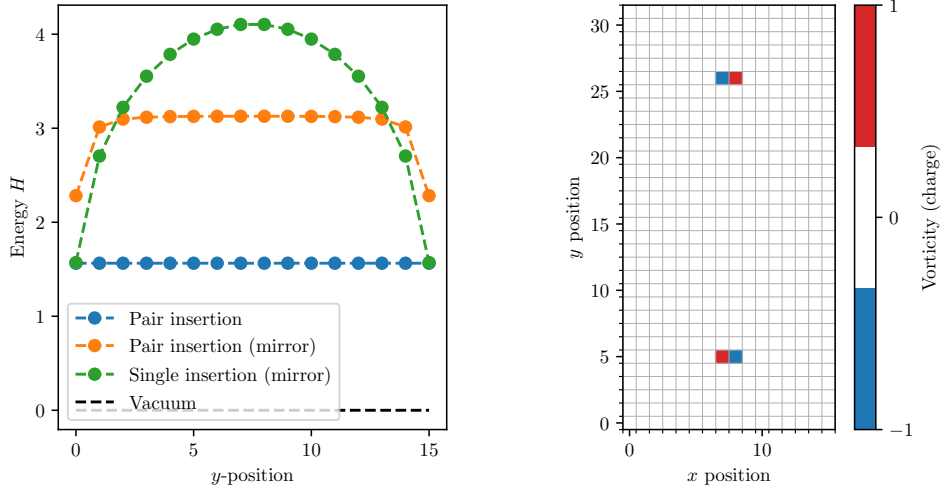


Figure 5.8: Left panel: The energy landscape of vortex-antivortex pair insertions and single vortex insertion ($\lambda = 4L$, $L = 16$ and the Fourier period is L). Right panel: A snapshot of the configuration for pair insertion (mirror) at y -position = 5. Dragging the pair from $y = 0$ to $y = 15$ generates the left energy landscape (analogously for regular pair insertion and single insertion (mirror)).

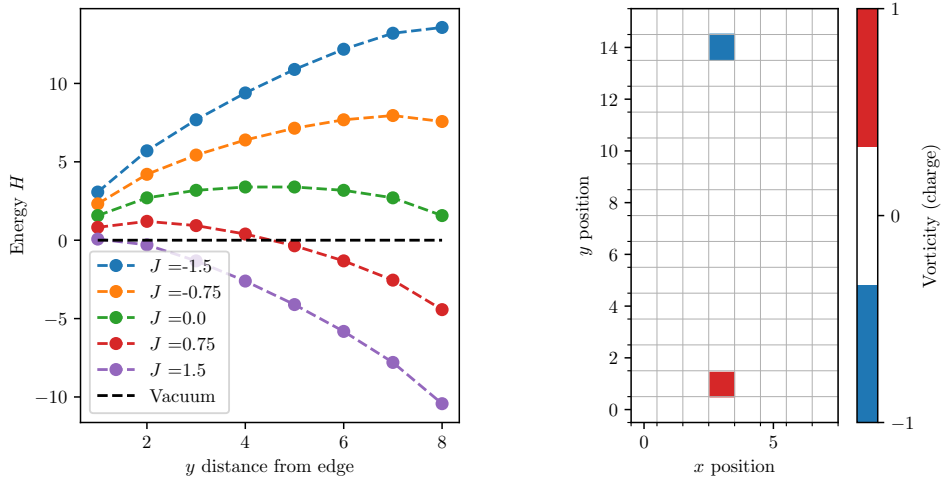


Figure 5.9: Left panel: The energy landscape of a single vortex crossing the mirror system for different supercurrents J . The system length is $L = 8$, penetration length $\lambda = 4L$ and Fourier period L . Right panel: A snapshot of the configurations used to generate the energy landscape, here the y distance from edge is 1.

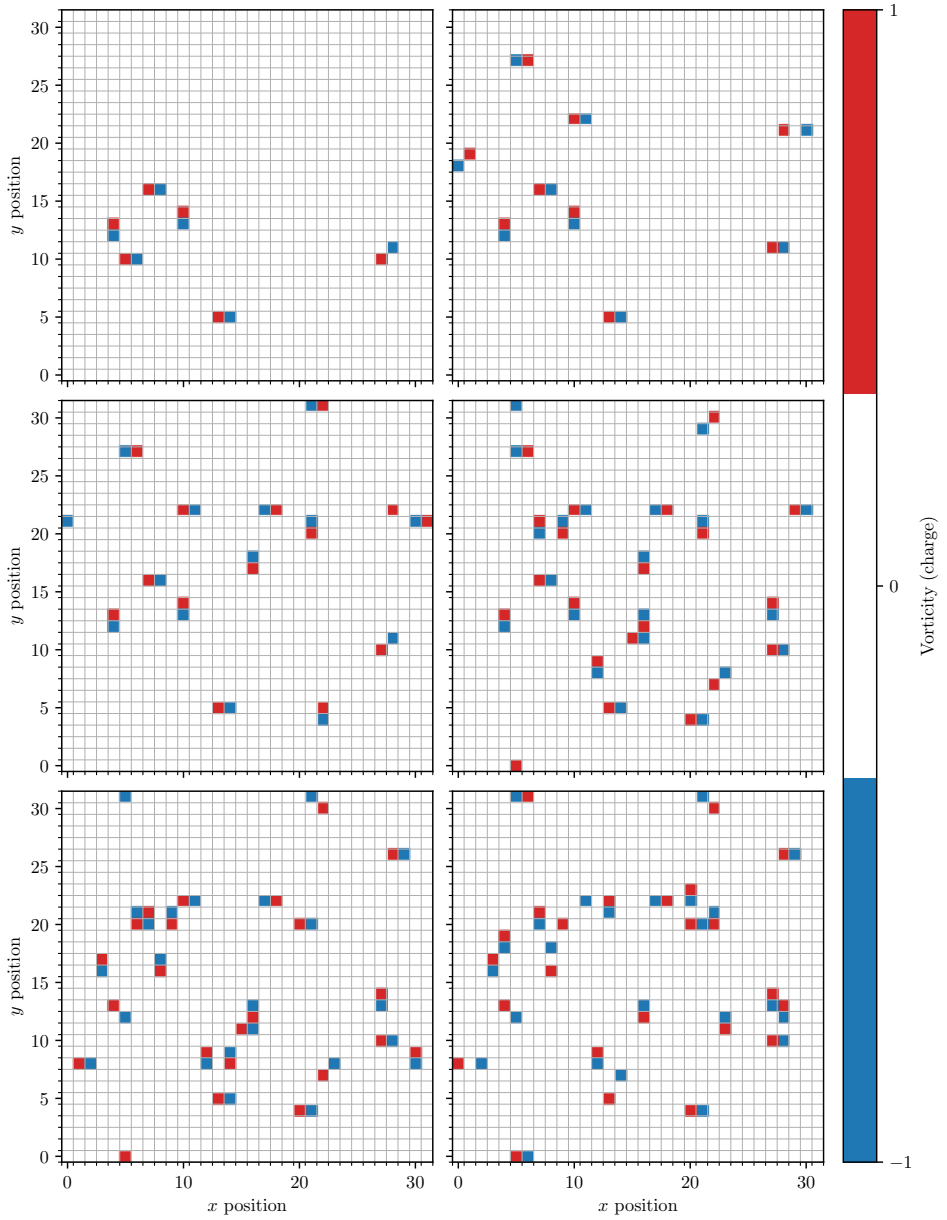


Figure 5.10: Snapshots for film PBC $T = 0.3$, $J = 0$ for every sweep 1, 2, \dots 6 (read left to right, row by row).

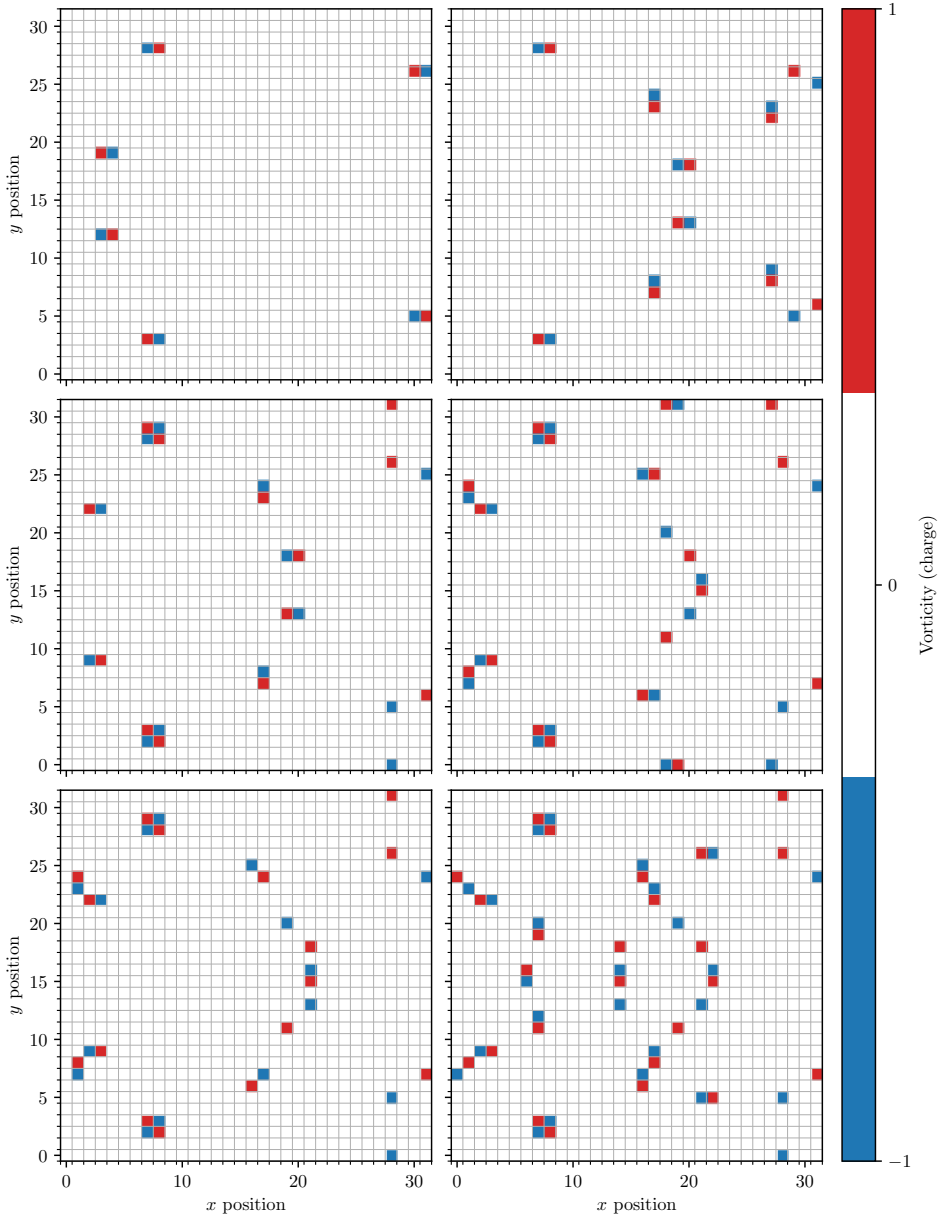


Figure 5.11: Snapshots for wire OBC $T = 0.5$, $J = 0$ for every sweep 1, 2, \dots 6 (read left to right, row by row). Both mirror and physical configurations are shown.

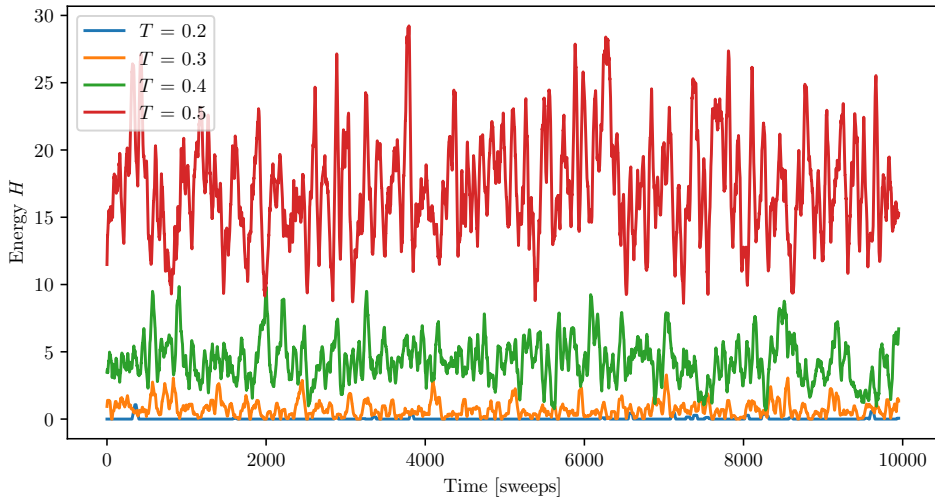


Figure 5.12: Wire OBC: moving average (width 50 sweeps) of the energy over time when $J = 0$, $L = 16$ for different temperatures.

Table 5.1: A time benchmark for looping the MC algorithm for periodic boundary conditions (PBC) and open boundary conditions (OBC) implemented on a laptop with the `timeit` command. It gives a mean \pm std. dev. of 7 runs. The system size $L = 16$ and does not affect the time per MC step significantly.

	Time for 10^6 MC steps	Time per MC step
PBC	1.84 s \pm 19.2 ms	1.84 μ s \pm 19.2 ns
OBC	12.7 s \pm 216 ms	12.7 μ s \pm 216 ns

the system is in equilibrium. Furthermore, the particle flow Q_y is also interesting which behaves as random walk in the case $J = 0$ and high enough temperatures T .

Finally, let us take a look at the actual computation time. Implemented in Python on a laptop, it can be seen that 10^6 MC steps takes around 1 second for PBC and around 10 seconds for OBC for $L = 16$ (Table 5.1). The explanation for this is that the system with OBC has a double system size and the energy calculations for this is somewhat more. Then, simulating a 16×16 system with 10^4 sweeps at a particular temperature should take 4.7 seconds for PBC and 33 seconds for OBC. Of course, these times are heavily dependent on the computer specifications but give a rough order of magnitude of these calculations. For a 16×16 system, around 10^7 and 10^6 sweeps can be calculated on a laptop over the course of a day.

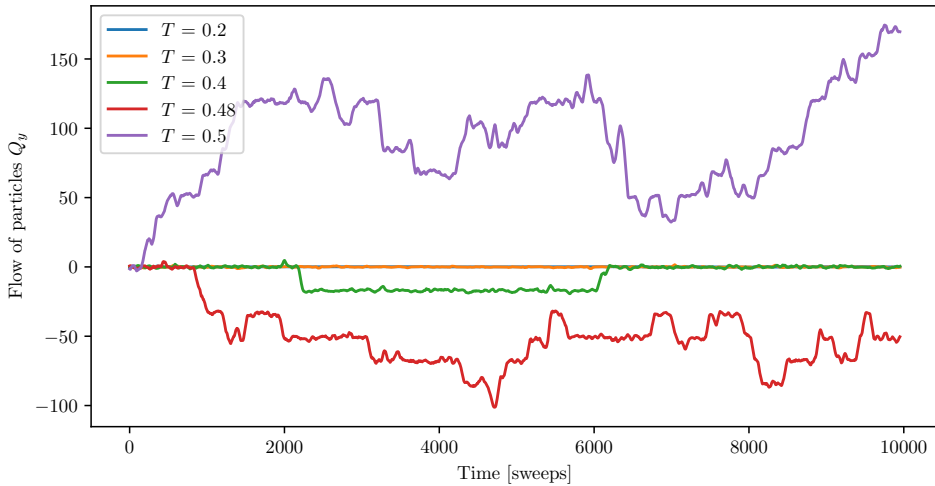


Figure 5.13: Wire OBC: flow over time when $J = 0$, $L = 16$ for different temperatures.

5.4 Equilibrium properties

The equilibrium properties of the 2D Coulomb gas can be determined as time averages of the Monte Carlo data, e.g. average energy, average number of particles and particle flow. Of course, there will be an initial transient before reaching the equilibrium state which at a first look is smaller than a few hundred sweeps. In this section, the time average quantities are presented for both OBC (wire) and PBC (film), measured during 10^4 sweeps and with an initial transient of 10^3 sweeps that are discarded.

The time averages are calculated over a range of both temperature and system sizes. For all Monte Carlo simulations, the same potential V is calculated with a screening length $\lambda = 4L$ and Fourier period of L , for both PBC (film) and OBC (wire). Furthermore, $J = 0$ since otherwise the system will be driven into a non-equilibrium which will be further analyzed later. The system sizes presented here are for PBC 4×4 , 8×8 , 16×16 and somewhat different for OBC where the system is split in two parts: one physical and one mirror configuration. For OBC the following physical system sizes are instead used: 4×8 , 8×16 , 16×32 .

The equilibrium properties of the 2D Coulomb gas model with PBC and OBC show clear similarities and differences (Fig. 5.14-5.16). Firstly, it can be seen that the number of particles per site and energy per site are correlated which would be expected (Fig. 5.14). For T around 0.2, it can be seen that the PBC shows clear excitation and suggests a phase transition in this region. However, for the wire (OBC), it seems that a phase transition occurs in the region $0.3 < T < 0.4$. The

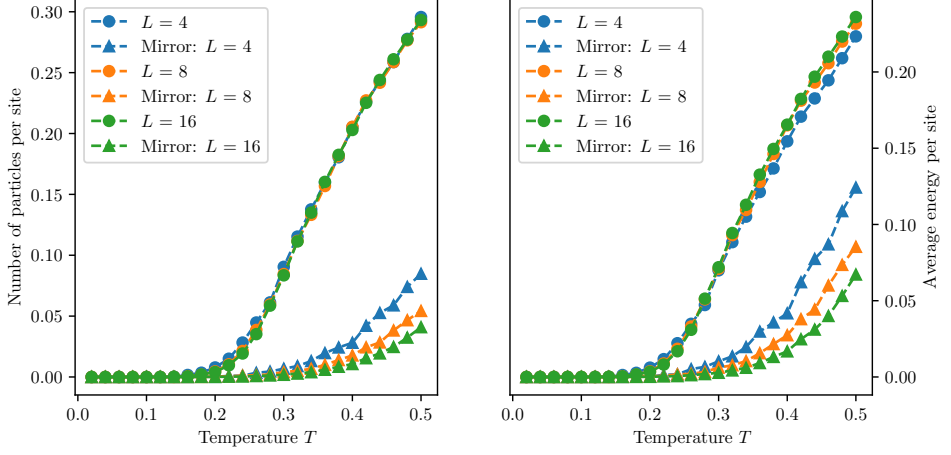


Figure 5.14: Time average per site quantities: number of particles and energy of the 2D Coulomb gas for different temperatures T . System size film PBC: $L \times L$. System size wire OBC: $L \times 2L$. 10^4 sweeps were used and 10^3 sweeps were discarded as a transient.

reason for this larger temperature region is likely that mirror configurations show a factor 2 increase in pair energies.

Likewise, the heat capacity also seems to be temperature-shifted for OBC compared to PBC (Fig. 5.15) and reached a peak around $T = 0.5$ and $T = 0.3$, respectively. The seeming temperature shift can also be seen in the resulting entropy per site, obtained by the integral $\int c/T dT$, which is non-decreasing and also gives $S = 0$ at $T = 0$ (Fig. 5.16). In contrast, the free energy decreases with T , as would be expected, but still shows clear differences between PBC and OBC (Fig. 5.16).

No conclusion about the critical temperature should however be drawn by a visual inspection. The critical temperature can only be determined in the limit where the system size becomes infinite, and it is clear that there are sizable finite-size effects for the OBC compared to PBC (Fig. 5.14). However, this will not be further analyzed here since the main target is not phase transition physics in the thermodynamic limit. Instead the aim is to consider the case of an applied supercurrent relevant for operation of SNSPD wire systems.

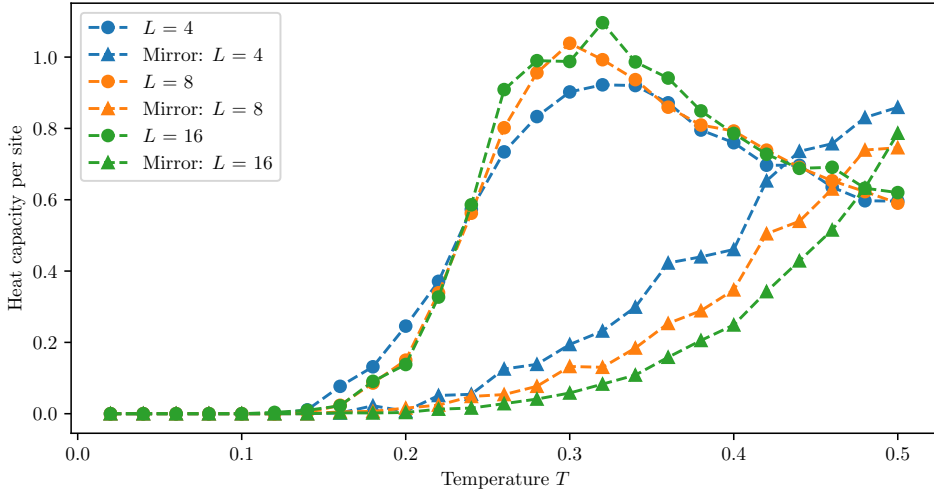


Figure 5.15: Heat capacity per site of the 2D Coulomb gas for different temperatures T . System size film PBC: $L \times L$. System size wire OBC: $L \times 2L$. 10^4 sweeps were used and 10^3 sweeps were discarded as a transient.

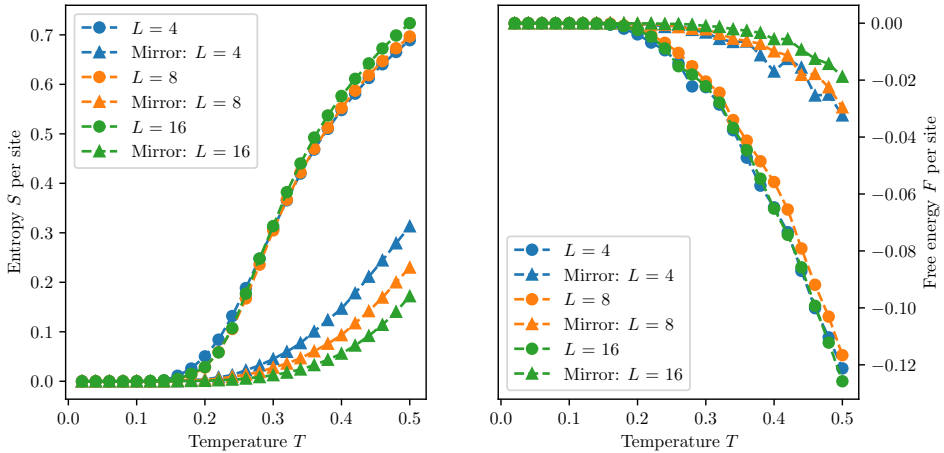


Figure 5.16: Entropy and free energy of the 2D Coulomb gas for different temperatures T . System size film PBC: $L \times L$. System size wire OBC: $L \times 2L$. 10^4 sweeps were used and 10^3 sweeps were discarded as a transient.

5.5 Applied current and non-equilibrium properties

In the case $J \neq 0$, the system is expected to be driven to a non-equilibrium steady state which also is observed for high enough J (Fig. 5.17, 5.18). The sign of J determines the direction of particle flow in the y direction; $J > 0$ drives positive particles downward and negative particles upward and vice versa for $J < 0$. In particular, the critical current is expected to be $|J_c| = 1.57$ at $T = 0$, since, from before, this will drive single vortices across the system. Indeed, focusing on OBC, this is what is observed in simulation snapshots (Fig. 5.17). For larger T , this value of J can be lower and still drive vortices across the system (Fig. 5.18).

The simulation snapshots show vortices crossing the system, but this can also be quantified by measuring the particle flow Q_y , i.e. counting the number of pair insertions in the y direction. Positive charges moving upward and negative charges moving downward are counted positively and negatively vice versa. This particle flow Q_y can then be used to calculate the mean voltage $V = Q_y/(tL_y)$ and mean electric field $E = Q_y/(tL_xL_y)$ (Fig. 5.19-5.21).

In particular, for OBC, it can be seen that there is no substantial particle flow for small T and J , e.g. $T < 0.22$ at $J = 0.3$ (Fig. 5.19) where Q_y fluctuates around 0. However, for large enough T and J , vortices start to cross the entire system, giving sudden transitions of $L + 1$ (Fig. 5.19). The time averages of these Q_y then give a non-zero mean-voltage. For even larger T , the particle flow increases even more, resulting in larger mean voltages V (Fig. 5.20). For temperatures larger than 0.4, Q_y increases approximately linear with time (Fig. 5.21).

However, these results are specific for the specific values of T and J . A more insightful analysis is given by computing the mean of the voltage V , dividing by L_x to get a normalized electric field $E = V/L_x$ which is plotted against the supercurrent J . This is an example of an IV characteristic. In a loglog plot, both PBC and OBC show similar IV characteristics, where the curves converge for $J > 1$ independent of temperature (Fig. 5.22). These statistics were calculated for 10^5 sweeps. A clear difference between PBC and OBC is that the OBC electric field E is about one order of magnitude smaller than for PBC.

Furthermore, the same data can be compared to $E \sim \exp(-C(J_c/J)^\mu)$, where $\mu = 1$ and C a constant. In a semilog plot of E and J^{-1} , this is expected to give a straight line where J_c can be estimated, which is only approximately observed in the data. Approximate straight lines can indeed be observed for large J^{-1} (Fig. 5.23). The relationship is only expected to hold in the limit $J^{-1} \rightarrow \infty$ but it is in this realm where measurement is difficult; small J gives very small particle flow. The convergence is therefore slow.

Finally, the same data also provide an estimate of the critical current J_c at different temperatures. A large enough non-zero electric field E is indicative of a steady particle flow Q_y which breaks equilibrium. Setting, for instance, this limit to $E = 10^{-2}$ and finding the lowest J giving $E > 10^{-2}$, will be an estimate of

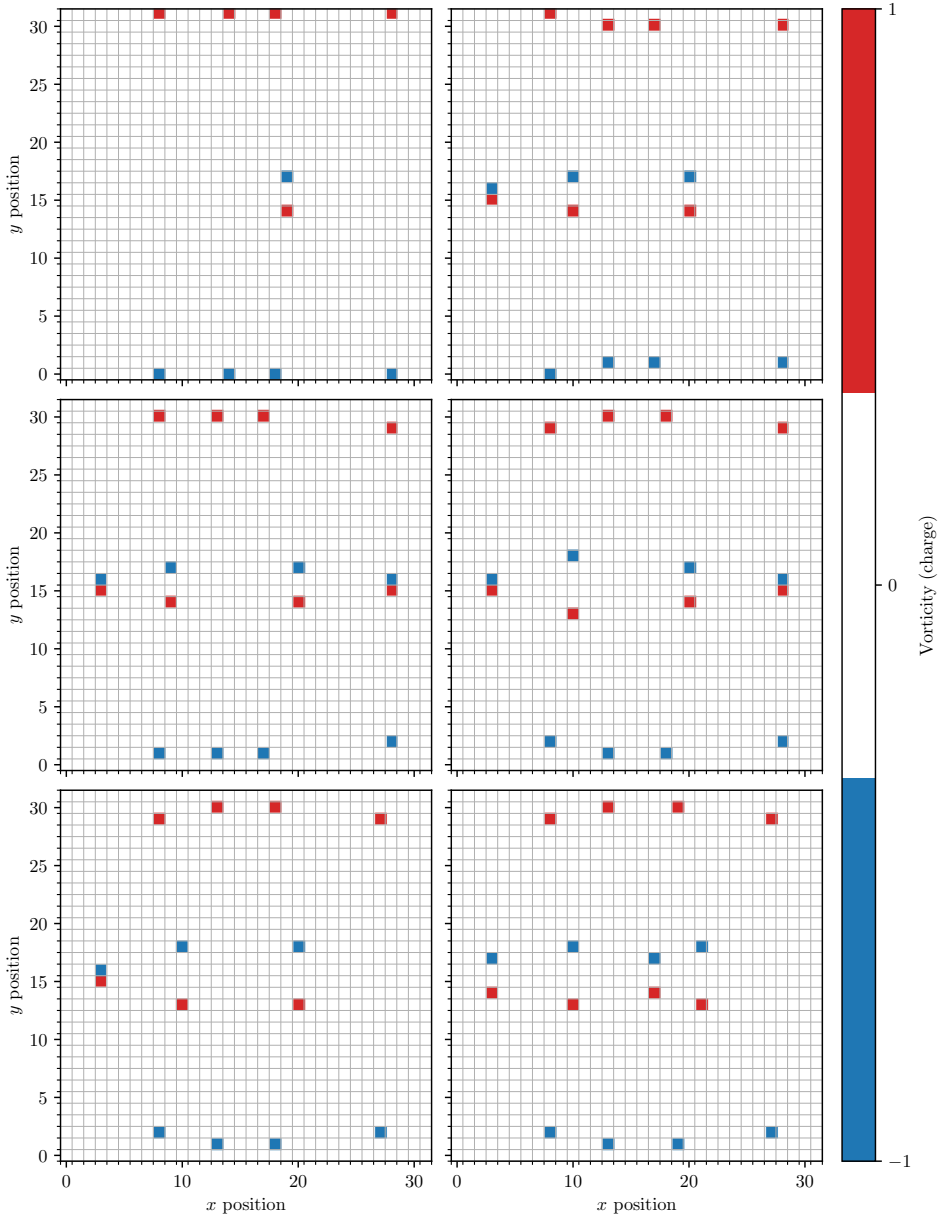


Figure 5.17: Snapshots for wire OBC $T = 0.1$, $J = 1.57$ (critical current for $T = 0$) for every sweep 1, 2, \dots 6 (read left to right, row by row). Positive charges move down and negative charges up.

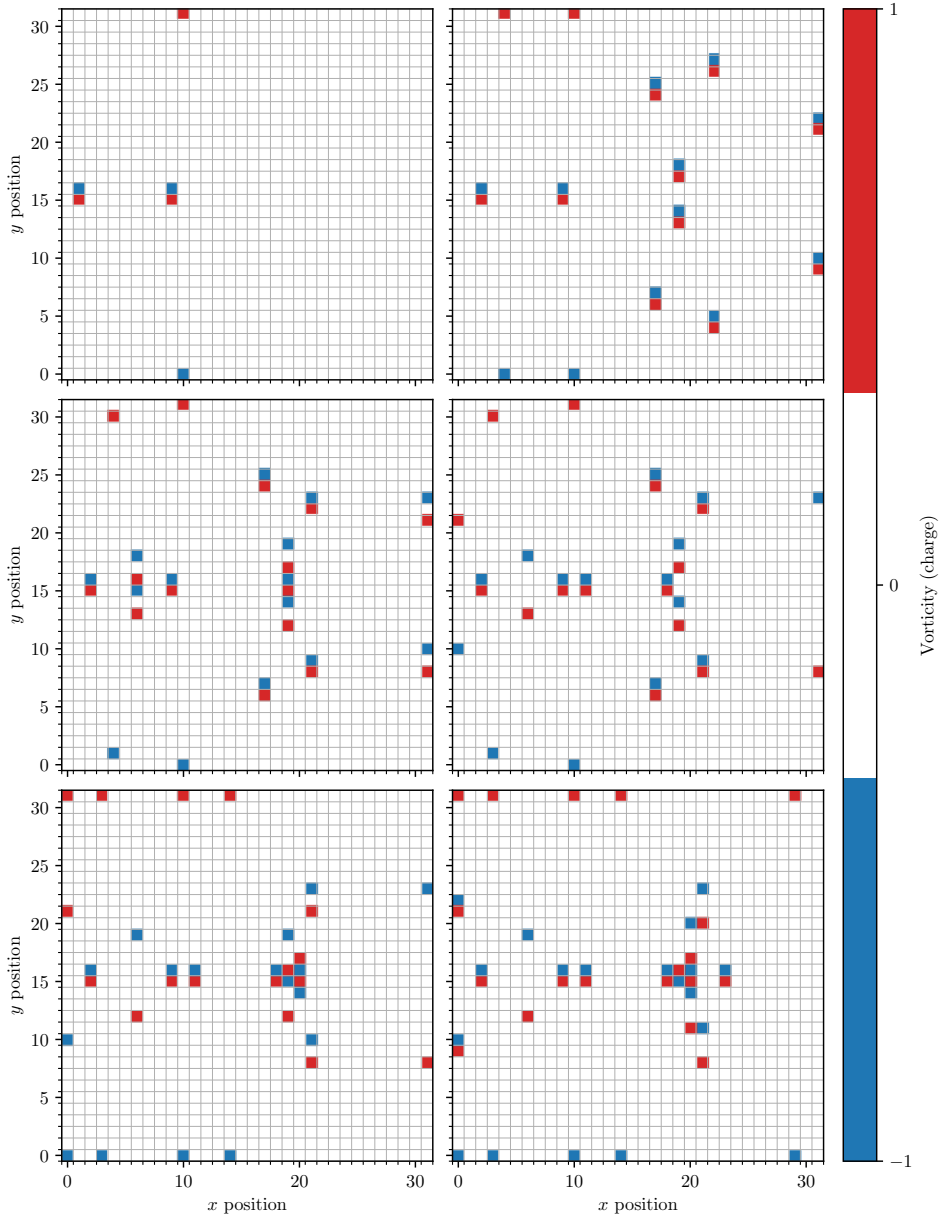


Figure 5.18: Snapshots for wire OBC $T = 0.4$, $J = 1$ for every sweep 1, 2, \dots 6 (read left to right, row by row). Positive charges move down and negative charges up.

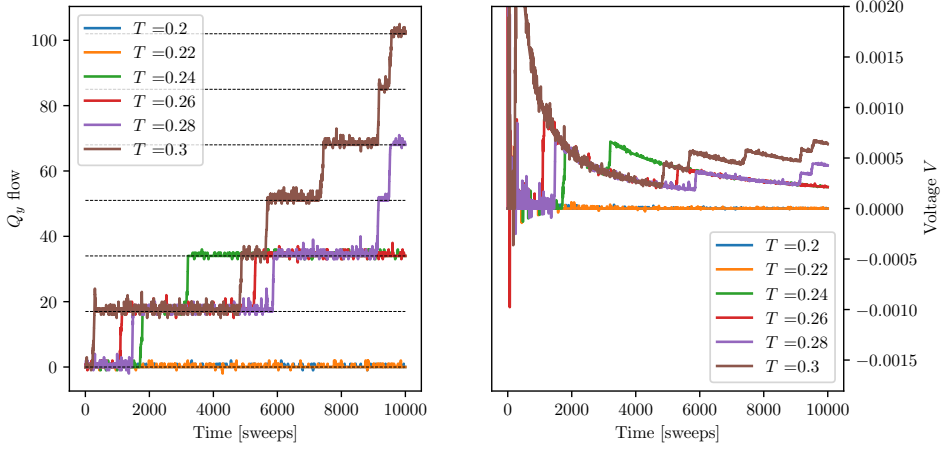


Figure 5.19: Particle flow Q_y over time when $J = 0.3$ for different temperatures. System size wire OBC: 16×32 .

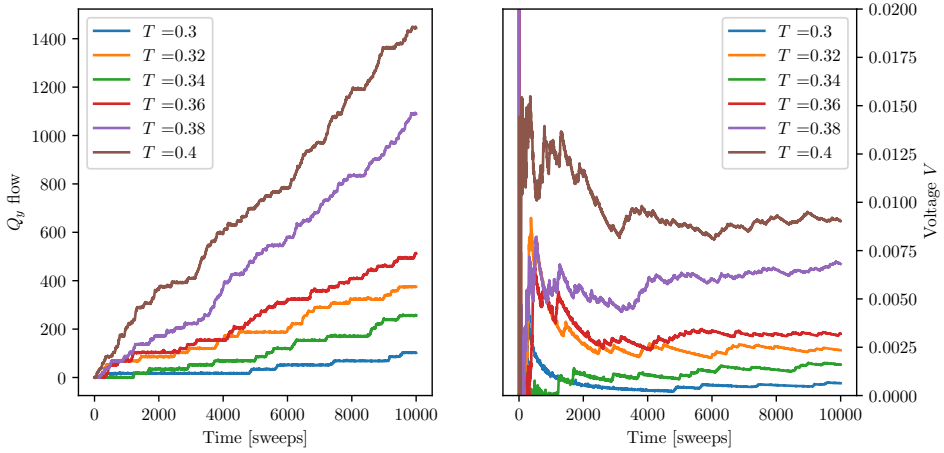


Figure 5.20: Particle flow Q_y over time when $J = 0.3$ for different temperatures. System size wire OBC: 16×32 .

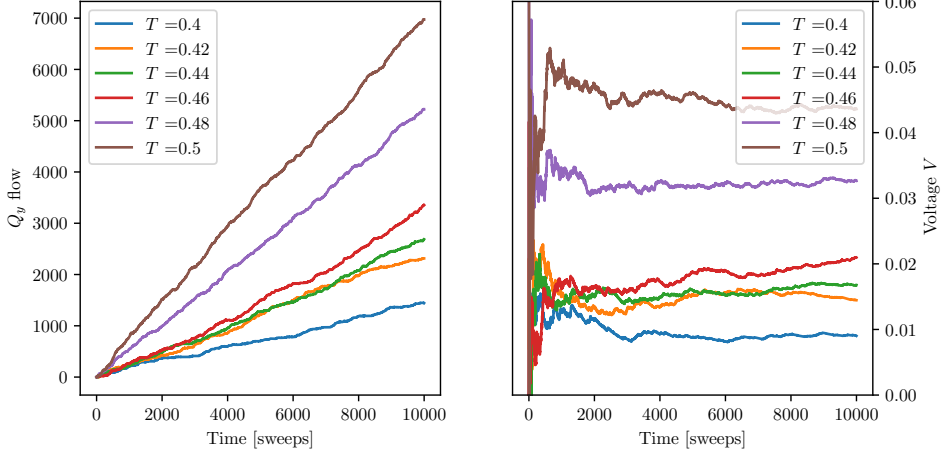


Figure 5.21: Particle flow Q_y over time when $J = 0.3$ for different temperatures. System size wire OBC: 16×32 .

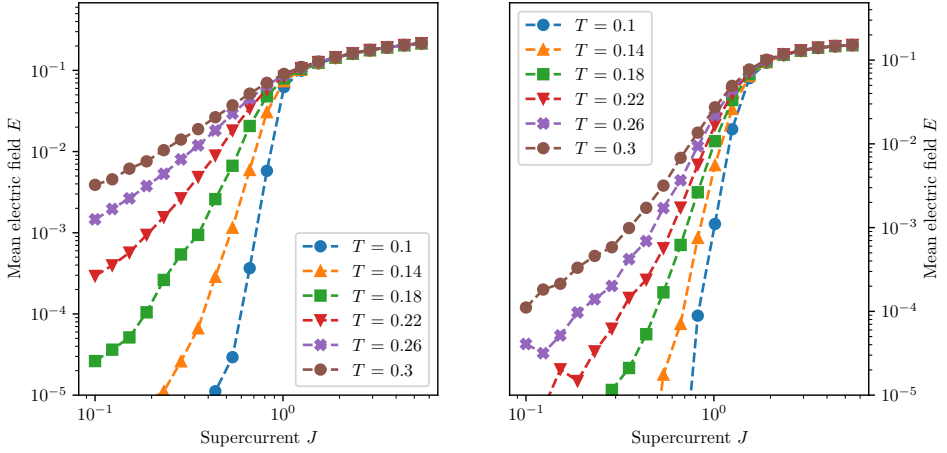


Figure 5.22: Left panel: Current electric field characteristics for PBC film system 8×8 . Right panel: Current electric field characteristics for OBC wire system 8×16 . 10^5 sweeps were used with 10^3 as a transient.

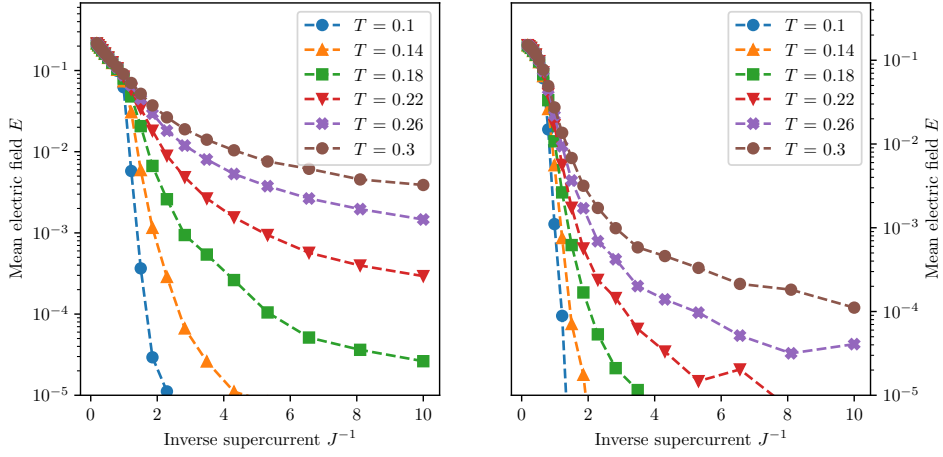


Figure 5.23: Left panel: Inverse current electric field characteristics for PBC film system 8×8 . Right panel: Inverse current electric field characteristics for wire OBC system 8×16 . 10^5 sweeps were used with 10^3 as a transient.

J_c . Then it is found that J_c decreases approximately linearly with temperature for both PBC and OBC (Fig. 5.24).

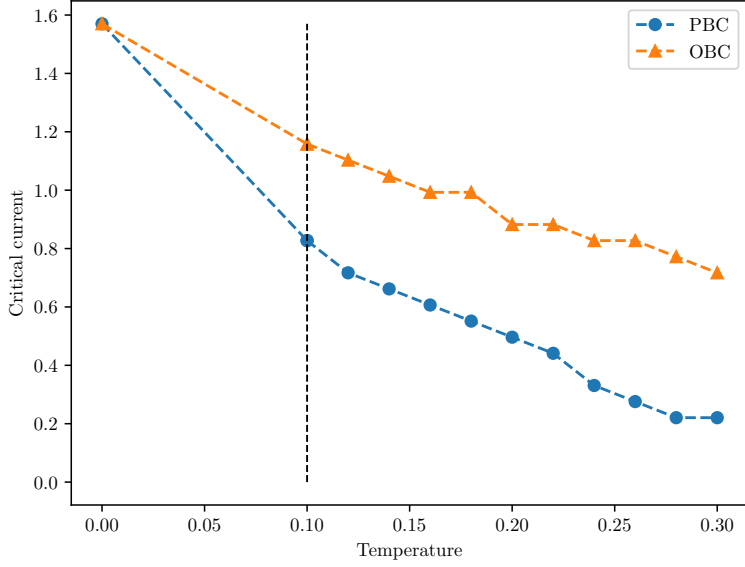


Figure 5.24: Estimation of critical current J_c for different temperatures T by finding the smallest J where electric field $E > 10^{-2}$. Interpolation of J was used to further improve this estimate. System size PBC (film): 8×8 . System size OBC (wire): 8×16 . Data was generated with 10^5 sweeps and 10^3 was used as transient.

Chapter 6

Summary and conclusions

In this thesis, a model for vortex dynamics in SNPDs has been proposed as an alternative to models formulated by the TDGL and GTDGL equations usually featured in simulations of these systems. This model, the 2D Coulomb gas, is derived from the XY model which in turn comes from as a special case of Ginzburg-Landau theory where the phase of the complex order parameter dominates and the magnitude can be assumed to be constant. It is a simplification that models vortices directly on a discretized lattice using Monte Carlo methods. Arguably, this simplification would be easier to implement and less computationally demanding in comparison to the integration of TDGL equations.

The 2D Coulomb gas is carefully constructed, analyzed and simulated in this thesis for both film geometry with periodic boundary conditions (PBC) and wire geometry with open boundary conditions (OBC). In particular, OBC are enforced using the method of images and a mirror system. A supercurrent J is also applied driving particle flow. Special attention is given to the Coulomb potential V which is part of every energy calculation of the model. The potential is calculated with a truncated Fourier series with a screening length λ which has a direct effect on the self energy of a single vortex $V(0)/2$. A convergence analysis shows agreement with this truncated series and the expected potential and that the choice $\lambda = 4L$ or greater gives a satisfactory convergence for our purposes. Furthermore, the pair energy of a neighbouring antivortex-vortex pair seems to converge to $\pi/2$ for $L \rightarrow \infty$.

Based on the potential V , energy landscapes were calculated for both PBC and OBC showing clear differences. Since the number of vortices are doubled, the self and pair energies also double far away from the edges. A naive assumption would be that the critical temperature also becomes larger with a factor 2, but that seems to not be the case. The energies of insertions closer to the edges are lower, especially for single vortices, and these boundary effects are not negligible, even for large systems.

The effect of an applied current J in the x direction is implemented with an energy contribution $\pm J$ that drives vortex movement in the y direction. This means that the Hamiltonian H is not only dependent on the vortex configuration, but also the path of single vortex movement in the y direction. This can also be explained by the loss of phase information by the transition to the Coulomb gas model from the XY model. An approximation of the critical supercurrent J_c at $T = 0$ is given by $J_c = 1.57 \approx \pi/2$ which cancels out the self energy of a single vortex in the mirror configuration.

The Monte Carlo simulations of the 2D Coulomb gas model show promising results. Transient analysis shows a transient smaller than a few hundreds sweeps in the case of $J = 0$. The transient is also of the same order when J becomes larger, but for small $J > 0$ many moves are rejected, making convergence more difficult and transient persist longer. The results of equilibrium properties, for $J = 0$, of PBC and OBC show clear differences. Qualitatively, many relationships are similar such as for the energy and heat capacity, except for a seeming change in temperature scale. However, the exact calculation of the critical temperature is difficult and outside the scope of this thesis to determine.

Furthermore, the particle flow for different supercurrents J were measured during the Monte Carlo simulations, giving a way to calculate the voltage over time of the system. It is this voltage which is measured in an actual SNSPD and detects an event, motivating a particular interest how this behaves in the 2D Coulomb gas model. An analysis of the IV characteristics shows overall expected behavior but clear differences between film and wire geometries – the wire geometry having smaller voltage for the same supercurrent and temperature. In addition, this also provides an estimate of how J_c changes for different temperatures, which is found to be approximately linear.

In conclusion, these results show promising potential of the 2D Coulomb gas as a model for SNSPDs that is both simple to implement and computationally efficient. Of course, these results provide many suggestions for further development such as the critical temperature of the mirror system with OBC as well as modeling direct photon absorption with this model. A real SNSPD also consists of meandering thin nanowires and for this reason it would be interesting to formulate the 2D Coulomb gas model in turns and non-square geometries. The possibilities are many.

The first SNSPD was created in 2001 and the development will only improve with better and more computationally efficient models. Today an SNSPD is commercially available for 100 000 euros which is likely to be reduced even more in the future, paving the way for applications in quantum optics and quantum cryptography. Although superconductors were discovered more than 100 years ago, they remain as important as ever in a broad range of applications. Our understanding of them continues to improve and will be a key building stone of the technology of tomorrow.

Bibliography

- [1] J. F. Annett *et al.* *Superconductivity, superfluids and condensates*, Vol. 5 (Oxford University Press, 2004).
- [2] V. V. Schmidt, P. Müller and A. V. Ustinov, *The physics of superconductors: Introduction to fundamentals and applications* (Springer Science & Business Media, 1997).
- [3] I. C. of Superconductivity, Nobel laureates in superconductivity, 2018.
- [4] A. D. Semenov, G. N. Gol'tsman and A. A. Korneev, *Quantum detection by current carrying superconducting film*, Physica C: Superconductivity **351**, 349 (2001).
- [5] C. M. Natarajan, M. G. Tanner and R. H. Hadfield, *Superconducting nanowire single-photon detectors: physics and applications*, Superconductor science and technology **25**, 063001 (2012).
- [6] I. Esmail Zadeh *et al.*, *Superconducting nanowire single-photon detectors: A perspective on evolution, state-of-the-art, future developments, and applications*, Applied Physics Letters **118**, 190502 (2021).
- [7] J. P. Allmaras *et al.*, *Demonstration of a thermally coupled row-column snspd imaging array*, Nano letters **20**, 2163 (2020).
- [8] A. Engel *et al.*, *Detection mechanism of superconducting nanowire single-photon detectors*, Superconductor Science and Technology **28**, 114003 (2015).
- [9] A. Söderstrand, Models of superconducting nanowire single-photon detection, 2017.
- [10] A. Schmid, *A time dependent Ginzburg-Landau equation and its application to the problem of resistivity in the mixed state*, Physik der kondensierten Materie **5**, 302 (1966).
- [11] L. P. Gor'kov, *Microscopic derivation of the Ginzburg-Landau equations in the theory of superconductivity*, Sov. Phys. JETP **9**, 1364 (1959).

- [12] L. P. GOR'KOV and G. Eliashberg, Generalization of the ginzburg-landau equations for non-stationary problems in the case of alloys with paramagnetic impurities, 30 Years Of The Landau Institute—Selected Papers, pp. 16–22, World Scientific, 1996.
- [13] M. Tinkham, *Introduction to superconductivity* (Courier Corporation, 2004).
- [14] S. Background, *Topological Phase Transitions and Topological Phases of Matter*, The Nobel Prize in Physics (2016).
- [15] M. E. Newman and G. T. Barkema, *Monte Carlo methods in statistical physics* (Clarendon Press, 1999).
- [16] L. P. Kadanoff, *Statistical physics: statics, dynamics and renormalization* (World Scientific, 2000).
- [17] J. Cserti, *Application of the lattice Green's function for calculating the resistance of an infinite network of resistors*, American Journal of Physics **68**, 896 (2000).
- [18] H. Lindström, New scaling method for the kosterlitz-thouless transition, 2016.
- [19] D. S. Fisher, M. P. A. Fisher and D. A. Huse, *Thermal fluctuations, quenched disorder, phase transitions, and transport in type-II superconductors*, Phys. Rev. B **43**, 130 (1991).
- [20] N. Metropolis *et al.*, *Equation of state calculations by fast computing machines*, The journal of chemical physics **21**, 1087 (1953).